

# Flow along a long thin cylinder

O. R. TUTTY

School of Engineering Sciences, University of Southampton, Highfield, Southampton SO17 1BJ, UK

(Received 20 March 2007 and in revised form 11 January 2008)

Two different approaches have been used to calculate turbulent flow along a long thin cylinder where the flow is aligned with the cylinder. A boundary-layer code is used to predict the mean flow for very long cylinders (length to radius ratio of up to  $O(10^6)$ ), with the effects of the turbulence estimated through a turbulence model. Detailed comparison with experimental results shows that the mean properties of the flow are predicted within experimental accuracy. The boundary-layer model predicts that, sufficiently far downstream, the surface shear stress will be (almost) constant. This is consistent with experimental results from long cylinders in the form of sonar arrays. A periodic Navier–Stokes problem is formulated, and solutions generated for Reynolds number from 300 to  $5 \times 10^4$ . The results are in agreement with those from the boundary-layer model and experiments. Strongly turbulent flow occurs only near the surface of the cylinder, with relatively weak turbulence over most of the boundary layer. For a thick boundary layer with the boundary-layer thickness much larger than the cylinder radius, the mean flow is effectively constant near the surface, in both temporal and spatial frameworks, while the outer flow continues to develop in time or space. Calculations of the circumferentially averaged surface pressure spectrum show that, in physical terms, as the radius of the cylinder decreases, the surface noise from the turbulence increases, with the maximum noise at a Reynolds number of  $O(10^3)$ . An increase in noise with a decrease in radius (Reynolds number) is consistent with experimental results.

---

## 1. Introduction

Axial flow along a long cylinder is relevant to a number of applications, including the flow along wire or thread, drawing of optical fibres, and the flow along towed sonar arrays which are used for underwater sensing. A sonar array may have a very large ratio of length to radius, up to  $O(10^5)$ , with a radius in the order of centimetres and a length of a kilometre or more. Currently there is a trend to develop smaller, more easily deployed devices, using, for example, optical fibres as sensors. However, the performance of towed arrays is usually limited by the noise generated by the turbulent fluctuations on the surface of the body (Knight 1996), and, for a given flow velocity (tow speed), decreasing the diameter of the array leads to an increase in the turbulent noise (Marschall *et al.* 1993; Potter *et al.* 2000). This process would not be expected to continue indefinitely, and one question addressed in this paper is how small the cylinder must be before the turbulent flow noise stops growing. The sensors on towed arrays are usually mounted along the axis of the cylinder, and measure averaged pressure in some form rather than point pressure, through a transfer function representing the transfer of the surface pressure fluctuations to the axis. The form of the transfer function will depend on the construction of the array and the configuration of the sensors, and will not be considered here (see Knight 1996

for a theoretical study of this effect). The work presented here is concerned mainly with behaviour quantities relevant to the performance of towed arrays. In particular, we will consider the variation of the wall mean shear stress and the circumferentially averaged wall pressure spectra with the Reynolds number of the flow. However, in addition to the spectra for circumferentially averaged wall pressure, some point spectra will be presented.

Flow along a cylinder has an additional length scale to that for a flat plate, the cylinder radius. If the boundary layer is thin compared to the radius, then the flow will resemble that on a flat plate, with negligible effect from the curvature of the wall. However, once the boundary thickness becomes comparable with the size of the cylinder, effects of curvature will be significant. The flow also depends on the Reynolds number, which is defined in terms of the cylinder radius  $a$  and free-stream velocity  $U_\infty$  so that  $Re = aU_\infty/\nu$ , where  $\nu$  is the kinematic viscosity of the fluid. We can also define  $a^+ = au_\tau/\nu$  where  $u_\tau = (\tau_w/\rho)^{1/2}$  is the friction velocity, with  $\tau_w$  the shear stress at the wall and  $\rho$  the density of the fluid.  $a^+$  gives the radius of the cylinder in wall units. It is also the Reynolds number using the friction velocity as the reference velocity. For  $y^+$  of  $O(a^+)$  or greater, where  $y^+$  is the distance from the surface in wall units, the effects of the curvature of the wall will be important. Closer to the wall, the effects of curvature will be less important. If  $a^+$  is large, the boundary layer near the surface should resemble that for a flat plate, with the curvature significant only in the outer part of the flow. For small  $a^+$ , the effects of curvature will be felt closer to the wall. In the laminar sublayer for a flat plate, we have  $u^+ = y^+$ , where  $u^+ = u/u_\tau$ , and  $u$  is the streamwise velocity. This reflects momentum equilibrium in the sublayer, given by  $\tau = \tau_w$ . For the cylinder, as noted by Glauert & Lighthill (1955) among others, the equilibrium model is  $r\tau = a\tau_w$ . This gives

$$u^+ = a^+ \log(1 + y^+/a^+). \quad (1.1)$$

Hence if  $a^+$  is  $O(1)$ , the effects of the wall curvature would extend right to the wall.

For the laminar problem, Seban & Bond (1951) give the first three terms in a series solution valid near the leading edge of the cylinder, giving expressions for the shear stress on the surface and the displacement area. Stewartson (1955) gives a series solution for very large distances along the cylinder. Stewartson shows that sufficiently far along the cylinder, the wall shear stress decays logarithmically with distance, rather than algebraically as is usually found. Glauert & Lighthill (1955) considered the flow along the entire cylinder. They developed a similar series solution to Stewartson for the flow far downstream. They produced a set of recommended curves for quantities such as the displacement area and the skin friction.

Tutty, Price & Parsons (2002) solved the problem of laminar boundary-layer flow on a cylinder numerically. They found good agreement with the predictions of Seban & Bond (1951) near the leading edge and Glauert & Lighthill (1955) far downstream. All these studies showed that there is an increase in the surface shear stress and a decrease in the boundary-layer thickness compared with those for a flat plate. Tutty *et al.* (2002) also considered the linear normal mode stability of the flow. They found that for Reynolds numbers less than 1060 the flow is unconditionally stable. This is in marked contrast to the flat-plate boundary-layer problem where the flow always becomes unstable if far enough downstream. Further, for the cases investigated, above the critical Reynolds number the flow was unstable for a finite distance only, reverting to stability further downstream, with closure of the neutral stability curves. Also, unlike planar flows, the two-dimensional (axisymmetric) mode was not the least

stable, but had only the fourth lowest critical Reynolds number. The mode with the lowest critical value was that with an azimuthal wavenumber of one.

The studies that exist for turbulent flow along a cylinder are mainly experimental, complemented by some attempts to obtain an appropriate form for a law of the wall. A substantial body of work comes from Lueptow and his colleagues (Lueptow, Leehey & Stellingner 1985; Lueptow & Haritonidis 1987; Lueptow 1988, 1990; Lueptow & Jackson 1991; Wietrzak & Lueptow 1994; Snarski & Lueptow 1995; Nepomuceno & Lueptow 1997; Bokde, Lueptow & Abraham 1999). These are experimental studies of flow with a Reynolds number of  $3 \times 10^3 - 5 \times 10^3$  with the boundary-layer thickness 5–8 times the cylinder radius. Lueptow (1988) is a review of much of the experimental work to that point. Willmarth *et al.* (1976) measured the boundary layer on vertically mounted cylinders with Reynolds numbers from 482 to 92 310 with the boundary-layer thickness from 1.88 to 42.5 times the cylinder radius.

Luxton, Bull & Rajagopalan (1984) investigated cylinders for Reynolds numbers from 140 to 785. Although the flow was unsteady for all Reynolds numbers, Luxton *et al.* (1984) observed that at the lowest Reynolds number,  $Re = 140$ , the high-frequency content of the flow was low, and argued that this flow was transitional rather than fully turbulent. They also observed that the turbulence intensities over most of the boundary layer were much lower than those expected on a flat plate, with peak values near the wall about twice that found on a flat plate. From this they suggested that the flow contained two scales, a fine wall scale with a gross outer scale forming most of the layer.

A series of experiments has been performed in a large towing tank (approximately 900 m in length) using thin cylinders aligned with the flow, with diameters of order 1 mm and lengths of order 100 m (Cippola & Keith 2003a; Furey, Cippola & Atsavapranee 2004) at relatively low Reynolds numbers ( $Re$  of  $O(10^3 - 10^4)$ ). A primary measurement in this work is the mean drag on the cylinders as a function of cylinder length, obtained by a direct measurement of the force on the body for cylinders of different lengths. From this, estimates of the momentum thickness at the ends of the cylinders are calculated. Furey *et al.* (2004) plot the mean wall shear stress against length for a cylinder with radius 0.445 mm for tow speeds from  $3.1 \text{ m s}^{-1}$  to  $14.4 \text{ m s}^{-1}$ . As far as can be seen from the plot (figure 6, Furey *et al.* 2004), there is no decay in the wall shear stress with the length of the cylinder, which varies from around 8 m to 150 m long.

As for laminar flow, the experimental studies show that the turbulent boundary layer on a cylinder has higher mean shear stress and is thinner than its counterpart on a flat plate. One observation is that the outer flow acts like a continuously regenerated wake rather than a boundary layer attached to a wall (Denli & Landweber 1979; Luxton *et al.* 1984; Lueptow & Haritonidis 1987; Wietrzak & Lueptow 1994).

The only numerical studies related to turbulent axial flow on a cylinder that we are aware of are those by Neves, Moin & Moser (1994) and Neves & Moin (1994). This work is also reported in Neves *et al.* (1992) which contains more detail. Rather than a spatially developing boundary layer with zero pressure gradient, Neves *et al.* considered a model problem, periodic in the streamwise direction, with a fixed boundary-layer thickness, and with a ‘mild streamwise pressure gradient’ to suppress the spatial growth of the boundary layer. We note that for a laminar flow, a non-zero pressure gradient can be introduced to suppress the boundary-layer growth, or more precisely, to fix the boundary-layer thickness. However, the streamwise velocity and pressure gradient cannot be constant, but must develop either spatially downstream or in time.

A number of studies consider the surface wall pressure spectra, although for relatively thin boundary layers (2–11 times the cylinder radius). Also, usually the spectra are for pointwise pressure measurements rather than the circumferentially averaged pressure found with towed sonar arrays. Willmarth & Yang (1970) give experimental spectra for a cylinder with  $Re = 115\,000$  and a boundary-layer thickness ( $\hat{\delta}$ ) of approximately  $2a$ , and Willmarth *et al.* (1976) a cylinder with  $Re = 36\,800$  and  $\hat{\delta} \approx 4a$ . Bokde *et al.* (1999) give measurements for a cylinder with  $Re = 3300$  and  $\hat{\delta} = 4.81a$  and Snarski & Lueptow (1995) measurements for a cylinder with  $Re = 3644$  and  $\hat{\delta} = 5a$ . Statistics on the pressure fluctuations from the numerical study by Neves *et al.* (1994) are presented in Neves & Moin (1994). They found that as the curvature increases (in effect, the Reynolds number and hence the size of the cylinder decreases) the root-mean-square (r.m.s.) pressure fluctuations decrease. This does not, as such, contradict the observation that the surface noise from the turbulence increases as the Reynolds number decreases, since the Reynolds numbers used by Neves & Moin (1994) are two to three orders of magnitude less than those for sonar arrays.

Since a sonar array may have a length to radius ratio of up to  $O(10^5)$ , it is not possible to perform a full Navier–Stokes calculation for such a configuration. Instead, first we will investigate the axial flow along a cylinder using a boundary-layer approach with the effects of the turbulence included through a turbulence model. This model will be validated by detailed comparison with experimental results. It will then be used to investigate the far-downstream behaviour of the flow. The predictions made, including that of essentially constant wall shear stress, are shown to agree with experimental results. Based on the results from the boundary-layer analysis, a model problem is then formulated. This problem is periodic in the streamwise direction, and can be solved numerically, using a Navier–Stokes solver for lower Reynolds numbers (5000 or below), and a large-eddy simulation (LES) approach for higher Reynolds numbers (up to  $5 \times 10^4$ ). The results from these calculations agree with experimental observations and the results from the boundary-layer model. The effect of the Reynolds number on the pressure spectra is then investigated.

## 2. Boundary-layer model

### 2.1. Formulation

The flow takes the form of a boundary layer with zero pressure gradient so that the governing equations in polar coordinates  $(x, r)$ , which are normalized by the cylinder radius  $a$ , are

$$\frac{\partial u}{\partial x} + \frac{1}{r} \frac{\partial}{\partial r}(rv) = 0, \quad (2.1)$$

$$u \frac{\partial u}{\partial x} + v \frac{\partial u}{\partial r} = \frac{1}{Re} \frac{1}{r} \frac{\partial}{\partial r} \left( r \frac{\partial u}{\partial r} \right) - \frac{1}{r} \frac{\partial}{\partial r}(r\overline{u'v'}), \quad (2.2)$$

where  $(u, v)$  are the streamwise and radial mean velocity components,  $(u', v')$  are the perturbation velocities, normalized by the free-stream velocity  $U_\infty$ . As a result of the assumption that the rate of change in the streamwise direction is much smaller than that in the transverse direction, only one of the Reynolds stresses,  $-\overline{u'v'}$ , appears in the governing equations.

We make the standard assumption that the Reynolds stress is proportional to the rate of strain, that is

$$-\overline{u'v'} = \frac{1}{Re} \mu_t \frac{\partial u}{\partial r}, \quad (2.3)$$

where  $\mu_t$  is the turbulent viscosity, which is normalized by the molecular viscosity  $\mu$ . The boundary-layer equation (2.2) becomes

$$u \frac{\partial u}{\partial x} + v \frac{\partial u}{\partial r} = \frac{1}{Re} \frac{1}{r} \frac{\partial}{\partial r} \left( r(1 + \mu_t) \frac{\partial u}{\partial r} \right). \quad (2.4)$$

The turbulent viscosity is calculated using the Spalart–Allmaras model (Spalart & Allmaras 1994). This model uses a single transport equation for a modified turbulent viscosity, with terms representing the generation, convection and destruction of the turbulent viscosity. The model used in this study is as given in Spalart & Allmaras (1994), adapted for an axisymmetric attached boundary layer. No additional tuning was performed, and the various damping functions and constants are as given by Spalart & Allmaras (1994).

A standard finite-difference scheme was used to solve the boundary-layer problem. Details of procedure used for the boundary-layer equations ((2.1) and (2.4)) can be found in Tutty *et al.* (2002). A Crank–Nicolson method was used for the turbulent viscosity equation.

The radial coordinate was scaled using

$$r = (1 + Re^{-1/2}hz), \quad (2.5)$$

where  $h = x^{2/3}$ . This scaling allows for the growth of the boundary layer. Note however, that this does not imply that the boundary layer grows as  $x^{2/3}$ . The growth of the boundary layer will be discussed below.

The grid in  $z$  was non-uniform, with the points clustered near the surface. The degree of stretch was adjusted to ensure that the grid point closest to the wall had  $y^+$  significantly less than one. The grid step in  $x$  was taken either as a constant or as  $x^{1/3}\Delta$  with  $\Delta$  usually taken as 0.005. The grid step in both directions was varied to check the accuracy of the solutions.

The flow near the leading edge was laminar and the boundary layer was tripped at a specified location. The position of the trip is not in itself important. Changing the position of the trip simply moves the position of the turbulent boundary layer along the cylinder, and away from the trip, results can be overlaid by adjusting the virtual origin of the turbulent flow.

Calculations were performed for a flat plate to verify that the code was producing the expected results. These were compared with the results from Spalart & Allmaras (1994), with excellent agreement.

## 2.2. Comparison with experimental results

In this section, predictions made using the turbulence model will be compared with experimental values found in the literature. Specifically, values taken from Willmarth *et al.* (1976) and Lueptow *et al.* (1985). Values for the experiments will be given in a mixture of units, matching those used in the source papers.

Willmarth *et al.* (1976) used a wind tunnel with speeds between 96 and 204 ft s<sup>-1</sup>, with cylinders of radius ranging from 0.01 to 1.0 in. This gave Reynolds numbers from 482 to 92310. The wind tunnel used was constructed specifically to study axial flow, with a vertical working section to avoid the sag which would be expected in experiments with very long, thin cylinders mounted horizontally. Willmarth *et al.* (1976) obtained flows with a large degree of axisymmetry. They did not trip the boundary layer, nor did they measure the position of transition. In order to compare the experimental results with the numerical values from the boundary-layer model, the calculations were terminated at the point where the boundary-layer thickness  $\hat{\delta}$

Case	$a$	$U_\infty$	$Re$	$\hat{\delta}$	$\hat{\delta}_1$	$\hat{\theta}$	$\hat{u}_\tau$	$\hat{\delta}_{1n}$	$\hat{\theta}_n$	$\hat{u}_{\tau n}$
1	0.010	96	482	0.425	0.0735	0.0630	6.65	0.0716	0.0689	5.55
2	0.010	147	736	0.375	0.0692	0.0591	9.20	0.0626	0.0602	8.08
3	0.010	180	899	0.240	0.0429	0.0327	11.30	0.0417	0.0396	9.68
4	0.020	145	1439	0.540	0.0791	0.0752	8.40	0.0904	0.0864	7.40
5	0.0625	142	4330	1.000	0.1780	0.1530	6.50	0.1658	0.1567	6.50
6	0.125	104	6203	1.302	0.2418	0.2237	4.56	0.2181	0.2023	4.61
7	0.125	160	9494	1.181	0.2042	0.1896	6.55	0.1942	0.1799	6.83
8	0.125	198	11693	1.165	0.1779	0.1657	7.73	0.1896	0.1758	8.29
9	0.250	105	12790	1.380	0.2233	0.1994	4.22	0.2274	0.2039	4.40
10	0.250	159	19230	1.178	0.1767	0.1573	6.21	0.1898	0.1690	6.44
11	0.250	192	23100	1.159	0.1703	0.1537	7.41	0.1847	0.1646	7.65
12	0.500	155	36680	2.062	0.3460	0.3040	5.75	0.3201	0.2844	5.95
13	1.000	158	74260	1.760	0.2770	0.2370	5.77	0.2629	0.2209	5.87
14	1.000	204	92310	1.880	0.2940	0.2340	6.98	0.2764	0.2342	7.42

TABLE 1. Experimental and numerical values for turbulent boundary layers. The values with subscript  $n$  are numerical, and the others are experimental from Willmarth *et al.* (1976). Lengths are in inches and velocities in  $\text{ft s}^{-1}$ .

matched that from the experiments, and the other values from the numerical solution at this point were compared with those measured by Willmarth *et al.* (1976). The boundary-layer thickness  $\hat{\delta}$  is based on  $0.99U_\infty$ .

Table 1 gives the test conditions for 13 different cases, as specified in Willmarth *et al.* (1976). Table 1 also gives the experimental values of the boundary-layer thickness  $\hat{\delta} = a\delta$ , and the experimental and numerical values of the displacement thickness  $\hat{\delta}_1 = a\delta_1$ , the momentum thickness  $\hat{\theta} = a\theta$ , and the friction velocity  $\hat{u}_\tau$ . Note that here and below, a circumflex will denote a dimensional quantity. The displacement and momentum thicknesses in non-dimensional form are defined as

$$(\delta_1 + 1)^2 - 1^2 = 2 \int_1^{1+\delta} (1 - u)r \, dr, \quad (2.6)$$

$$(\theta + 1)^2 - 1^2 = 2 \int_1^{1+\delta} u(1 - u)r \, dr, \quad (2.7)$$

respectively. Note that for consistency with Willmarth *et al.* (1976), for the numerical values given in table 1, the upper limit on the integral is set to  $1 + \delta$  rather than  $\infty$ .

Percentage differences between the experimental and numerical values for  $\hat{\delta}_1$ ,  $\hat{\theta}$  and  $\hat{u}_\tau$  are given in table 2. In Willmarth *et al.* (1976) the velocities were measured using a mixture of hot wires with three different lengths (0.005 in for cases 1–5, 0.019 in for cases 6–8, and 0.040 in for cases 9–11) and a pressure probe (cases 12–14). Generally, the experimental and calculated values of the displacement and momentum thickness show good agreement for cases 5–14, with poorer agreement for cases 1–4. However, for cases 1–4 the length of the hot wire is comparable to the radius of the cylinder, so relatively large errors could occur. The same length hot wire was used in cases 5 and 4. Unlike case 4, case 5 shows good agreement, but the cylinder in case 5 is more than three times as large as that in case 4.

The wall shear stress is given by  $\hat{\tau}_w = \rho \hat{u}_\tau^2$ , and hence the percentage difference between the experimental and numerical values for  $\hat{\tau}_w$  is approximately twice that given in table 2 for  $\hat{u}_\tau$ . Willmarth *et al.* (1976) state that the accuracy of their values for the wall shear stress is probably only  $\pm 10$  or 15%. Hence for cases 5–13 there

---

Case	$\hat{\delta}_1$	$\hat{\theta}$	$\hat{u}_\tau$
1	-2.5	9.4	-16.5
2	-9.5	1.9	-12.2
3	-2.8	21.0	-14.3
4	14.2	14.9	-11.9
5	-6.8	2.4	0.0
6	-9.8	-9.5	1.1
7	-4.9	-5.1	4.2
8	6.6	6.1	7.2
9	1.8	2.2	4.2
10	7.4	7.4	3.7
11	8.4	7.1	3.2
12	-7.5	-6.4	3.4
13	-5.1	-6.8	1.7
14	-6.0	0.1	6.3

---

TABLE 2. Difference between experimental and numerical values as a percentage:  
 $100(f_{num} - f_{exp})/f_{exp}$ .

---

is again good agreement between the experimental and calculated values of  $\hat{u}_\tau$ . The agreement is poorer for cases 1–4. However, it is not surprising that the agreement is not as good for the smaller cylinders. The experimental values for  $\hat{u}_\tau$  for cases 6–14 were obtained by direct measurement of the wall shear stress, while the values for cases 1–5 were obtained by fitting to the measured velocity profiles and extrapolating to the surface, assuming the velocity profile matched that for a planar boundary layer. This procedure was also used to estimate the distance from the surface of the measurement positions, since it was not possible to measure these with the accuracy required. The hot wires used to estimate the wall shear stress were very small, with the active part approximately 0.004 in (100  $\mu\text{m}$ ) long and 0.00001 in (0.25  $\mu\text{m}$ ) in radius. Relatively large errors in measurement could occur, compounded by the fact that for the very small cylinders the velocity profile differs from that for a flat plate, with no clear logarithmic region (see below). Also, Lueptow & Haritonidis (1987) performed a series of experiments for flow with Reynolds numbers from 1600 to 6400, where they measured the skin friction directly and estimated it using the same procedure as Willmarth *et al.* (1976). They found that Willmarth *et al.*'s method produced much larger values of the skin friction than those measured directly, especially at lower Reynolds numbers.

Figure 1 shows velocity profiles for cases 2, 5 and 13 along with experimental values taken from Willmarth *et al.* (1976). Figure 1 uses wall units, i.e. shows  $u^+ = \hat{u}/\hat{u}_\tau$  against  $y^+ = (r-1)a\hat{u}_\tau/\nu = ya^+$ . There is excellent agreement between the experimental and numerical results for cases 5 and 13. For case 2, figure 1 shows an apparently large difference. However, this is largely a reflection of the difference in the numerical and experimental values of  $\hat{u}_\tau$  (see tables 1 and 2).

The experimental and numerical values for  $a^+$  and  $\delta^+$  are given in table 3. The percentage difference in the values is the same as for  $\hat{u}_\tau$  in table 2. From the values for  $a^+$ , it can be seen that for case 13, the effects of the wall curvature should be restricted to the outer part of the boundary layer, and a large portion of the boundary layer should be similar to that for a flat plate. The velocity profile shown for case 13 in figure 1 shows the expected pattern, with a clear logarithmic region. There is also evidence for the loss of the shoulder in the far field characteristic of a planar

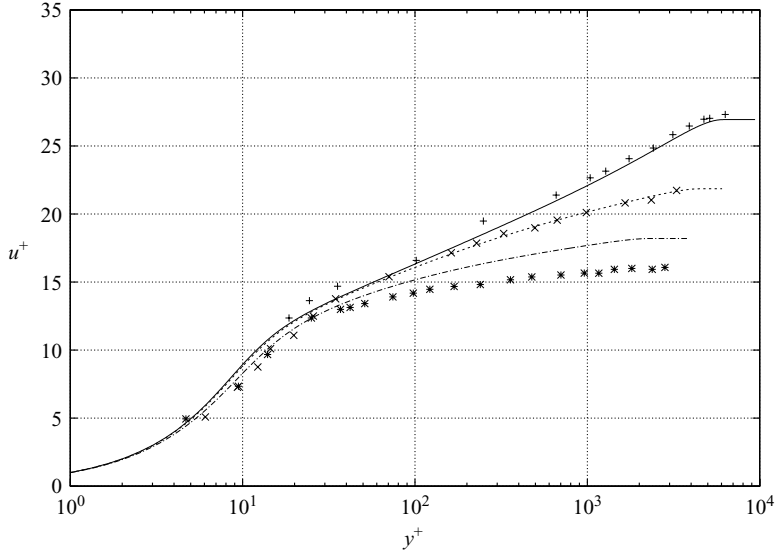


FIGURE 1. Velocity profiles in wall coordinates ( $u^+ = \hat{u}/\hat{u}_\tau$  against  $y^+ = (r-1)a\hat{u}_\tau/\nu$ ). Lines are numerical and symbols experimental from Willmarth *et al.* (1976): lower, case 2; middle, case 5; top, case 13.

---

Case	$a_e^+$	$a_n^+$	$\delta_e^+$	$\delta_n^+$
1	33.4	27.9	1419	1184
2	46.1	40.5	1727	1517
3	56.4	48.3	1355	1160
4	83.4	73.4	2251	1983
5	198.2	198.2	3171	3171
6	272.0	275.0	2833	2864
7	388.7	405.3	3672	3829
8	456.5	489.6	4255	4563
9	513.6	536.0	2835	2959
10	751.2	778.9	3539	3670
11	891.4	920.4	4132	4267
12	1360.7	1408.0	5612	5807
13	2709.6	2758.9	4769	4856
14	3158.0	3357.6	5937	6312

---

TABLE 3. Values of  $a^+ = a\hat{u}_\tau/\nu$ : experimental,  $a_e^+$ , from Willmarth *et al.* (1976); numerical,  $a_n^+$ . Also given are the corresponding values of  $\delta^+ = \hat{\delta}\hat{u}_\tau/\nu$ .

boundary layer. Experimental results (Lueptow *et al.* 1985) show that as  $a^+$  decreases, the velocity profile may have a logarithmic region, but the slope will be lower. The numerical solutions for the cases with the larger Reynolds numbers and values of  $a^+$  (cases 9–14) showed this. For the lower Reynolds numbers, the values of  $a^+$  are such that the effects of curvature should be important in the region that normally contains the logarithmic velocity profile. Both the numerical and experimental results reflect this, with initially a decrease in slope and then the loss of the logarithmic layer, as can be seen for cases 2 and 5 in figure 1. Luxton *et al.* (1984) studied the flow at low Reynolds number ranging from 140 to 785 and found that in this range the logarithmic region had completely disappeared.

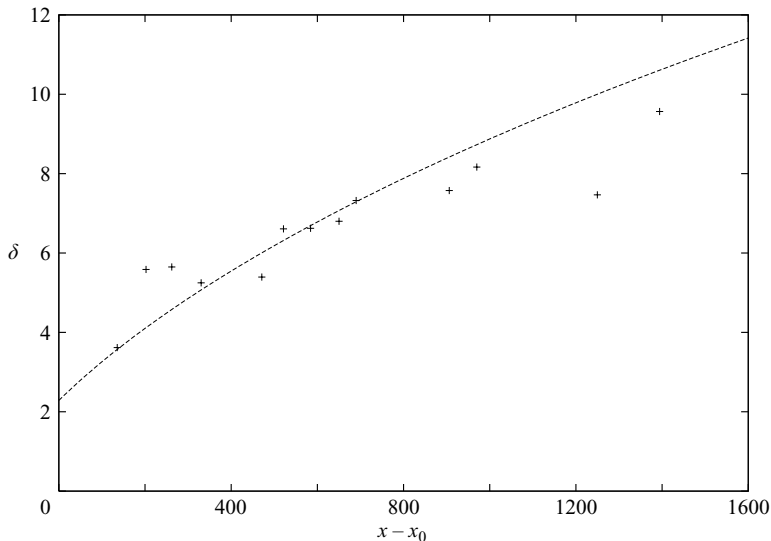


FIGURE 2. Non-dimensional boundary-layer thickness  $\delta$  against non-dimensional distance  $x - x_0$  (normalized on the radius  $a$ ) for a cylinder with  $a = 0.2375$  cm and  $U_\infty = 20$  m s $^{-1}$ . Line, numerical; symbols, experimental (Lueptow *et al.* 1985).

Lueptow *et al.* (1985) also performed experiments on a small circular cylinder, concentrating on the thick turbulent boundary layer where transverse curvature effects should be significant. They presented results for cylinders with Reynolds numbers from  $10^3$  to  $5 \times 10^3$ , approximately. Here we will use the results for a cylinder of radius 0.2375 cm with free-stream velocities of 20 or 30 m s $^{-1}$ , i.e. for Reynolds numbers from  $3 \times 10^3$  to  $5 \times 10^3$ , approximately. The cylinder was mounted horizontally, and the sag at the midpoint was 1.2 radii. Whereas Willmarth *et al.* (1976) used different sized cylinders and measured the boundary layer at the same point physically along the cylinder to obtain values for different regimes, Lueptow *et al.* (1985) measured it at different points on the same cylinder. For the cases we will consider, Lueptow *et al.* tripped the boundary layer using an 0.08 cm radius O-ring. Also, Lueptow *et al.* state that for this cylinder with a flow speed of 20 m s $^{-1}$ , there was a uniform streamwise pressure gradient of  $-10$  Pa m $^{-1}$  along the cylinder. This has been included in the numerical results presented here.

Figure 2 shows calculated and measured values for the boundary-layer thickness along the larger cylinder, and figure 3 the momentum thickness. In the experiments,  $x$  was measured as the distance from the trip. It is not possible to model directly the effects of such a large trip using a boundary-layer formulation. Instead, a virtual origin ( $x_0$ ) was used, estimated by approximately matching the apparent conditions at the trip indicated in figure 2 in Lueptow *et al.* (1985). This was done in two ways. First, the laminar boundary layer was allowed to grow to an appropriate thickness before it was tripped. Secondly, the boundary layer was tripped in the usual position, and the results displaced by an appropriate amount. Both approaches produced essentially the same results.

Figures 2 and 3 show good agreement between the numerical and experimental values except for those furthest downstream. However, in the experiments, the cylinder was mounted horizontally, and, as stated by Lueptow *et al.* (1985), the sag was sufficient to suggest that it may be modifying the boundary-layer thickness.

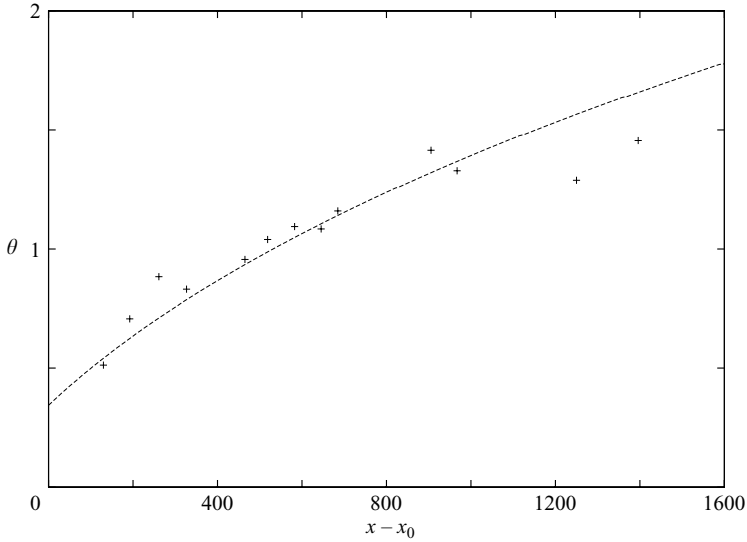


FIGURE 3. Non-dimensional momentum thickness  $\theta$  against non-dimensional distance  $x - x_0$  (normalized on the radius  $a$ ) for a cylinder with  $a = 0.2375$  cm and  $U_\infty = 20$  m s $^{-1}$ . Line, numerical; symbols, experimental (Lueptow *et al.* 1985).

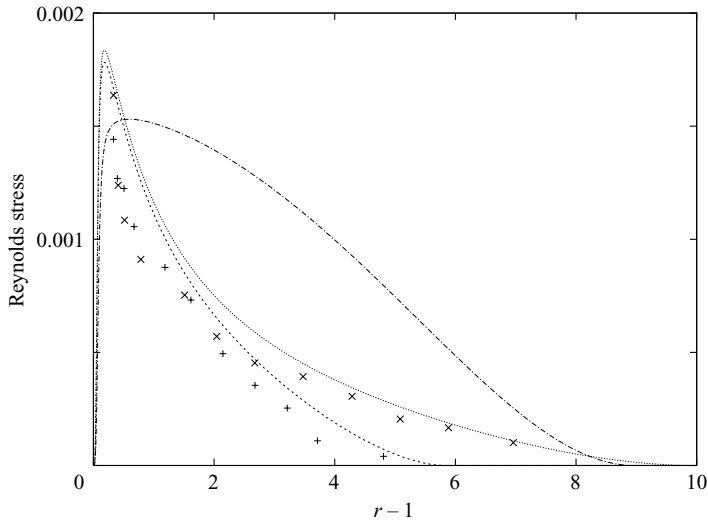


FIGURE 4. Non-dimensional Reynolds stress ( $-\overline{u'v'}$ ) against distance across the boundary layer ( $r - 1$ ) for a cylinder with  $a = 0.2375$  cm and  $U_\infty = 20$  m s $^{-1}$ . The top line gives the numerical results for a flat plate with  $\delta = 7.57$ , the middle line the cylinder with  $\delta = 7.57$  and the lower line the cylinder with  $\delta = 4.69$ . The symbols are experimental values for a cylinder from Lueptow *et al.* (1985) with  $\delta = 4.69$  (+) and  $\delta = 7.57$  (x). Distances are normalized by  $a$  and Reynolds stress by  $\rho U_\infty^2$ .

In particular, the effect of sag would be to thin the boundary layer toward the downstream end of the cylinder. The results presented in figures 2 and 3 are consistent with this.

Lueptow *et al.* (1985) gave plots of the Reynolds stress. Figure 4 compares numerical and experimental values of  $-\overline{u'v'}$  for  $U_\infty = 20$  m s $^{-1}$ . Also shown are the predicted

values of the Reynolds stress for an equivalent case on a flat plate, which are consistent with flat-plate experimental values (see Lueptow *et al.* 1985). There is a marked difference in the Reynolds stress distribution between the cylinder and the plate, with larger values near the wall and a faster drop off away from the wall. The numerical and experimental distributions for the cylinder have the same shape, but the numerical predictions are, in general, higher than the experimental values. However, we note that Lueptow & Haritonidis (1987) state that the measurements of the Reynolds stress reported in Lueptow *et al.* (1985) were made by a probe with poor spatial resolution.

The experimental values collapse onto a single curve near the wall ( $r - 1 < 2$ ), but separate further away from the wall, reflecting the growth of the boundary layer. The numerical values also show this behaviour. A comparison was made between the experimental and numerical values for  $U_\infty = 30 \text{ m s}^{-1}$ , with similar results.

Lueptow *et al.* (1985) also give values for the friction velocity  $\hat{u}_\tau$  obtained from a curve fit to the experimental results, and from matching the mean velocity profile to that expected for a flat plate. There was a significant difference between the two sets of values obtained in this way (up to 40%). The values we predict show good agreement with those obtained in Lueptow *et al.* (1985) by matching the velocity profile to the flat-plate one. With  $U_\infty = 20 \text{ m s}^{-1}$ , the experimental values range between  $\hat{u}_\tau/U_\infty = 0.053$  where  $\delta = 4.69$  and  $0.049$  where  $\delta = 8.11$ . The respective numerical values are  $0.0488$  and  $0.0496$  (the slight increase with  $x$  is due to the effect of the favourable pressure gradient). At  $30 \text{ m s}^{-1}$ , the experiments gave  $\hat{u}_\tau/U_\infty = 0.048$  at  $\delta = 5.59$  and  $0.047$  at  $\delta = 8.53$ . The equivalent numerical values are  $0.0460$  and  $0.0455$ .

The comparisons made above have shown that simulations using the Spalart–Allmaras turbulence model can faithfully reproduce the major features of a turbulent boundary layer along a cylinder, at least for the flow regimes for which detailed experimental measurements are available. As well as reflecting the differences between the boundary layer of a plate and a cylinder, given the uncertainty in experimental values, there is a large measure of quantitative agreement between the numerical and experimental results. In the next section, the code will be used to investigate the behaviour of the flow along cylinders with a range of Reynolds numbers.

### 2.3. Results

Numerical predictions for the non-dimensional wall shear stress,

$$\tau_w = \frac{\partial u}{\partial r}(x, 1), \quad (2.8)$$

near the leading edge of the cylinder with  $Re = 10^5$  are shown in figure 5. Also shown in figure 5 are the numerical values for a flat plate with the same reference Reynolds number. The boundary layer was tripped at  $x = 10$ . Upstream of this, as expected, there is little difference in the values for the cylinder and the flat plate. However, as soon as the boundary becomes turbulent the two sets of results diverge, with higher skin friction for the cylinder.

Figure 6 shows the boundary-layer thickness  $\delta = \hat{\delta}/a$  against  $x$  for  $Re = 10^5$ . Once the flow is tripped, the boundary layer grows rapidly, and is of the same size as the cylinder before  $x = 80$ . By this stage, the effects of the transverse curvature will be significant, as can be seen in figure 5. As for the laminar case, the boundary layer is thinner with higher wall shear stress than the equivalent flat-plate flow.

Figures 7 and 8 are similar to 5 and 6, but cover a much larger distance. The difference between the flat plate and cylinder flows increases downstream. Also, for

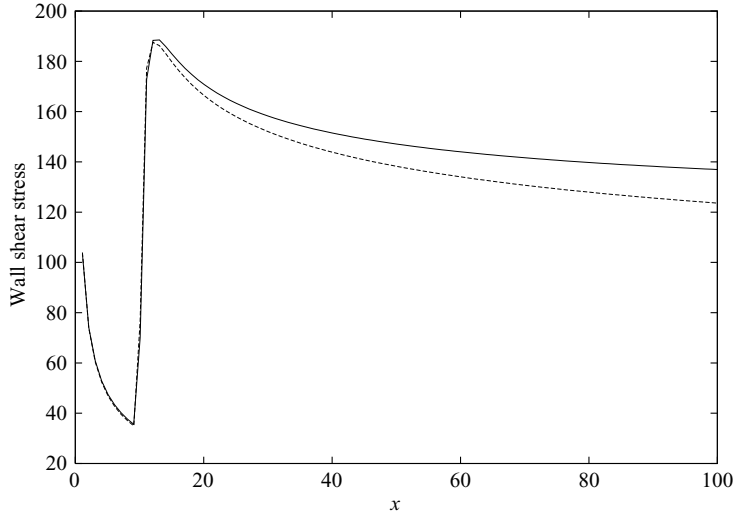


FIGURE 5. Non-dimensional wall shear stress (in units of  $\mu U_\infty/a$ ) versus distance (in units of the cylinder radius  $a$ ) for  $Re = 10^5$ . —, cylinder; ---, flat plate.

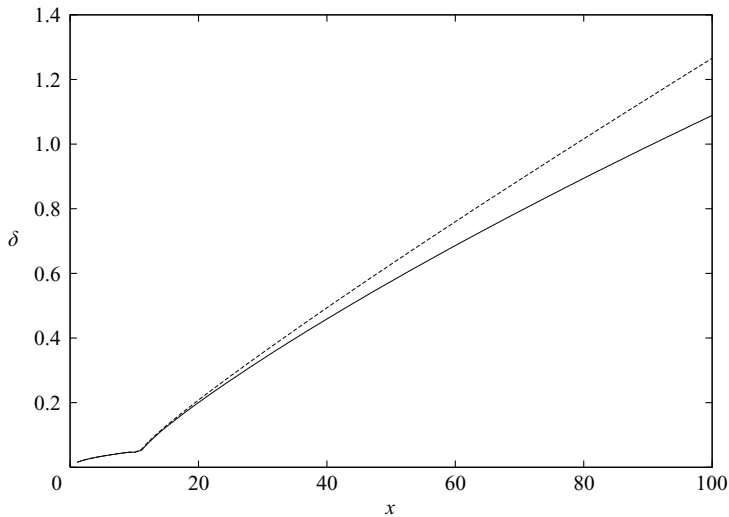


FIGURE 6. Boundary-layer thickness  $\delta$  versus distance along the cylinder  $x$  (in units of the cylinder radius  $a$ ) for  $Re = 10^5$ . —, cylinder; ---, flat plate.

the cylinder, the wall shear stress appears to tend to a constant value. However, a calculation was performed for a much longer run, until  $x = 10^5$ , and there was still a slow decay in the predicted value of the wall shear stress for the far downstream portion of the cylinder. It was not possible to determine whether this decay would continue indefinitely, or whether the wall shear stress was tending asymptotically to a finite value. However, the decay was extremely slow; from  $x = 5 \times 10^4$  to  $10^5$  it was approximately 0.3%. Physically, in water, a non-dimensional length of  $5 \times 10^4$  with  $Re = 10^5$  would represent a length of approximately 1 km for a cylinder with a radius of 2 cm and a free-stream velocity of  $5 \text{ m s}^{-1}$ , a typical speed for a sonar array. In

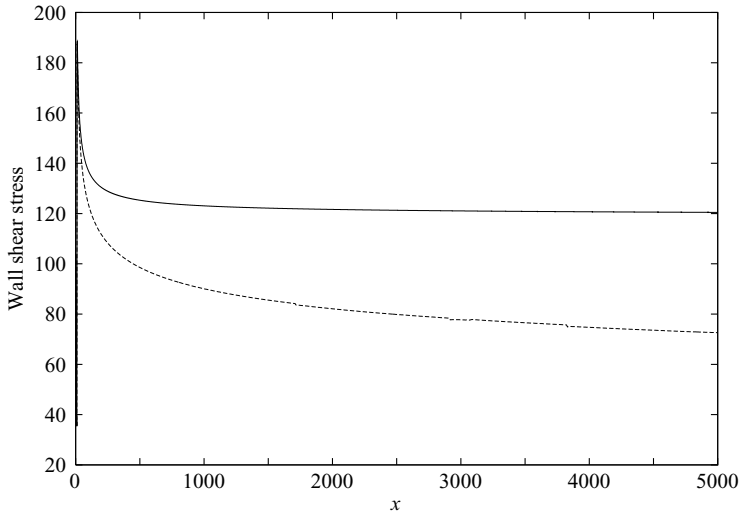


FIGURE 7. Non-dimensional wall shear stress (in units of  $\mu U_\infty/a$ ) versus distance (in units of the cylinder radius  $a$ ) for  $Re = 10^5$ . —, cylinder; ---, flat plate.

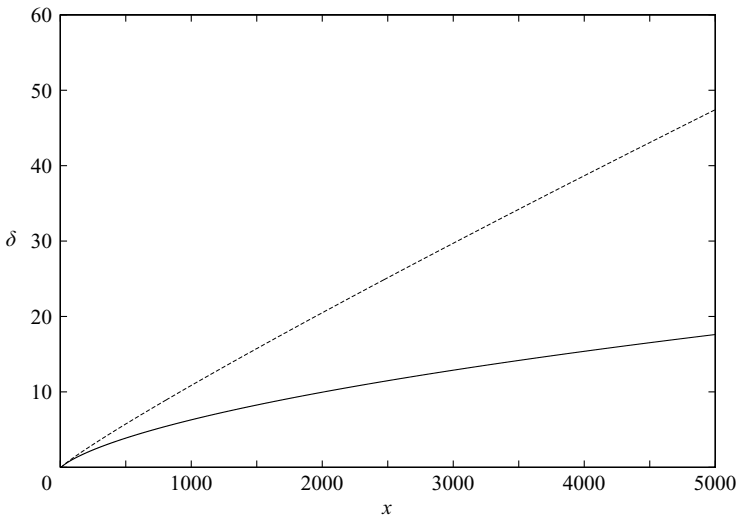


FIGURE 8. Boundary-layer thickness  $\delta$  versus distance along the cylinder  $x$  (in units of the cylinder radius  $a$ ) for  $Re = 10^5$ . —, cylinder; ---, flat plate.

air, the length would be approximately 2.5 km for a 5 cm radius cylinder with a flow of  $30 \text{ m s}^{-1}$ .

For all practical purposes, and within the limits of the expected accuracy of such calculations, for  $Re = 10^5$  the boundary-layer model is predicting that the wall shear stress is constant, except near the leading edge. Calculations were performed for a range of Reynolds numbers from 1 to  $10^6$ . The results were similar to those for  $10^5$ , with a thinner boundary layer and higher surface wall shear stress for the cylinder than for the flat plate, and with the wall shear stress tending to a constant, or almost constant, wall shear stress far downstream. Lueptow & Haritonidis (1987) measured the wall shear stress along a cylinder for a number of flow speeds and

used the data to produce a fit of the variation of  $\tau_w$  with  $Re_x$ , the Reynolds number based on the distance along the cylinder from the point the boundary layer was tripped. This gave a weak dependence on distance, with the friction coefficient given by  $C_f = 0.0123 Re_x^{-0.08}$ . However, for each of the three flow speeds used to produce this fit, the data could be interpreted as showing an initial drop in  $\tau_w$ , followed by an extended region where there is little change (see Lueptow & Haritonidis (1987), figure 6), consistent with the pattern shown in figure 7.

Furey *et al.* (2004) investigated the effects of the cylinder length on the mean drag for a cylinder of radius 0.445 mm and lengths from around 8 to 150 m by direct measurement of the force exerted on the cylinders. They present results for four flow speeds from 3.1 to 14.4 m s<sup>-1</sup>. An unexpected result is that there are fluctuations in the drag rather than a decrease with length (this was also reported in Cippola & Keith (2003a) where similar results with fewer data points are presented). No explanation of this effect was given. Although the values fluctuate, there is no apparent overall decay in the level of the wall shear stress for any of the flow rates in the data shown in Furey *et al.* (2004). The data for the largest flow rate (14.4 m s<sup>-1</sup>) was digitized and a linear regression analysis was performed. Within the accuracy of this procedure, the slope was zero. In fact, by dropping one value from the data set (the last one) the slope changed from a very small negative value to a small positive one. The mean value of the wall shear stress values shown in figure 6 of Furey *et al.* (2004) was estimated as 430 M m<sup>-2</sup>. By comparison, the estimate from the boundary-layer code was 395 N m<sup>-12</sup>, within 10%. There was a similar level of agreement for the other flow speeds (the numerical values are 179 N m<sup>-12</sup> for  $U_\infty = 9.3$  m s<sup>-1</sup>, 63 N m<sup>-12</sup> for  $U_\infty = 5.2$  and 25 N m<sup>-12</sup> for  $U_\infty = 3.1$ ).

Below, we will refer to a constant wall shear stress to refer to a representative value of the wall shear stress in the region where there is little or no variation over a long distance (much less than 1% over a non-dimensional distance of at least 10<sup>4</sup>). It is important to note, however, that there may still be some change, and that this is a prediction obtained using a turbulence model, although one that has been shown to behave well for this particular application.

The Reynolds stress  $-\overline{u'v'}$  at  $x = 2 \times 10^4$  ( $\delta = 33.8$ ) and  $x = 10^5$  ( $\delta = 88.3$ ) for  $Re = 10^5$  is shown in figure 9. There is little difference between the Reynolds stress distribution at these two widely spaced points, except in the far field, reflecting the downstream growth of the boundary layer. Over most of the boundary layer, the level of the Reynolds stress is low, indicating that strong turbulence is found only in the near-wall region, and that the far field is behaving essentially as a laminar flow. Further, there is little if any spatial development of the flow near the wall. This effect can also be seen in the velocity distribution across the boundary layer (see below for  $Re = 10$ ).

For axisymmetric flow on a cylinder with zero pressure gradient, the momentum integral equation becomes

$$\frac{d}{dx} \int_1^\infty u(1-u)r dr = \frac{\tau_w}{Re}. \quad (2.9)$$

Hence, the wall shear stress tending to a constant implies that the momentum thickness will grow as  $x^{1/2}$  for large  $x$ . The boundary-layer thickness would also be expected to grow as  $x^{1/2}$ . As can be seen from figure 10, the results from the numerical solution support this.

Cippola & Keith (2003a) and Furey *et al.* (2004) used (2.9) with the experimental drag values to estimate the variation in momentum thickness with length of the

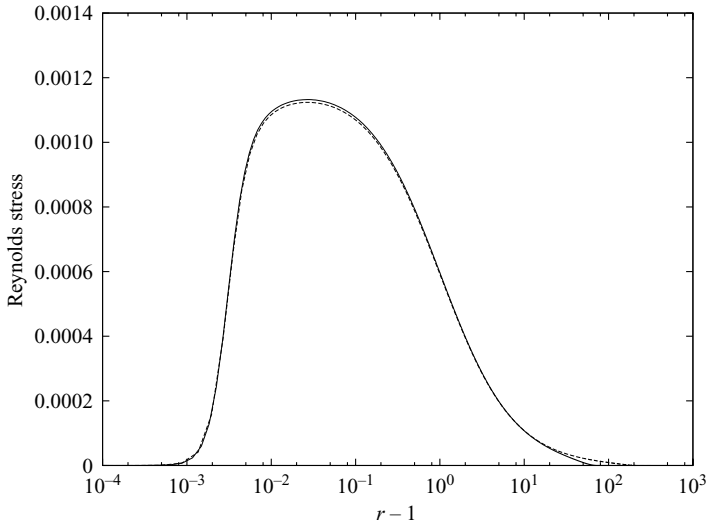


FIGURE 9. Reynolds stress  $-\overline{u'v'}$  (in units of  $U_\infty^2$ ) against distance across the boundary layer (normalized by  $a$ ) for  $Re = 10^5$ . The dashed line is for  $x = 2 \times 10^4$  and the solid line for  $x = 10^5$ .

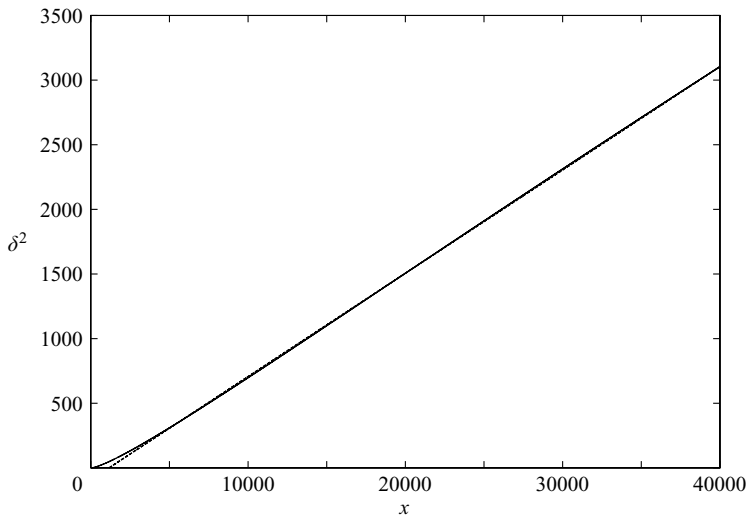


FIGURE 10. Boundary-layer thickness squared versus  $x$  (in units of  $a^2$  and  $a$ ) for  $Re = 10^5$ . Also shown is a straight line which is asymptotic to  $\delta^2$  for large  $x$ .

cylinder. There is little difference between the values obtained from (2.9) using the mean value of the experimental results and those plotted by Furey *et al.* (2004) obtained using the distribution of wall shear stress as a function of  $x$ . Also, Cippola & Keith (2003a) plotted the estimated values of the momentum thickness non-dimensionalized by  $\nu/\hat{u}_\tau$  against the momentum thickness Reynolds number, and noted that the apparent linear relationship could only be obtained if  $\hat{u}_\tau$  was constant.

As noted above, the smaller the value of  $a^+$ , the closer to the wall the effects of curvature will be felt. The smallest value of  $a^+$  for the data presented in Willmarth *et al.* (1976) or Lueptow *et al.* (1985) is 33.4 (table 3). This value is sufficiently large to

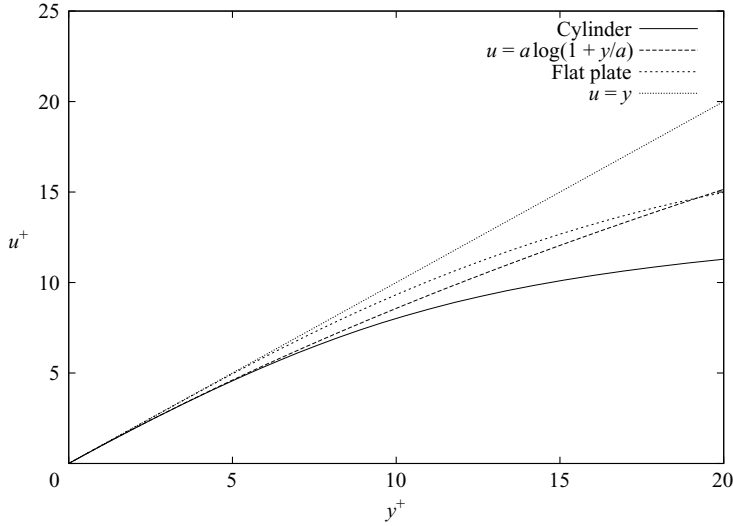


FIGURE 11. Velocity in wall units ( $u^+ = \hat{u}/\hat{u}_\tau$  against  $y^+ = (r-1)a\hat{u}_\tau/\nu$ ) close to the wall with  $Re = 482$ . This shows the numerical results for a cylinder (bottom curve) and a flat plate with the same value of the wall shear stress (second from top), plus the corresponding theoretical curves for the laminar sublayer.

suggest that the laminar sublayer should be similar to that for a flat plate. Figure 11 shows the numerical predictions for  $u^+$  against  $y^+$  for the cylinder for case 1 from Willmarth *et al.* (1976), and for a flat plate with the same value of the wall shear stress. Also shown are the profiles from (1.1) and from  $u^+ = y^+$ . For very small values of  $y^+$  (2 or less) these all produce essentially the same velocity profile. However, by  $y^+ = 5$  there is a noticeable difference between the velocity for the cylinder and the flat plate, and it is clear that by this stage, which is significantly less than  $y^+ = a^+$ , (1.1) provides a better comparison with the numerically generated velocity profile than the planar model.

Luxton *et al.* (1984) have performed experiments for flow with the Reynolds number as low as 140, which has  $a^+$  of approximately 13. The boundary-layer model produced a value of  $a^+$  of approximately 11 with the same boundary-layer thickness. Given the level of uncertainty, this level of agreement is as good as could be expected. There is, however, no data available that we are aware of in the literature for flows with  $a^+$  less than 10, when the effects of curvature would be expected to be significant right down to the wall. A calculation was performed with a very low value of the Reynolds number,  $Re = 10$ , which gave a far downstream value of  $a^+$  of 1.49. Figure 12 shows the wall shear stress. Again,  $\tau_w$  appears to tend to a constant as  $x \rightarrow \infty$ . Figure 13 shows the velocity in wall units at  $x = 10^6$  and  $2 \times 10^6$ , and the predicted near-wall behaviour from (1.1). There is little difference between the velocity at the two points except a long way from the cylinder, with agreement up to  $y^+$  at least  $10^3$ . The difference in the far field reflects the continuing growth in the thickness of the boundary layer. Note that since the scaling is the same for the two positions used in figure 13, the velocity in physical terms matches up to the same point, which is approximately 700 radii from the cylinder.

It can also be seen that (1.1) gives a good estimate for the velocity up to  $y^+ \approx 20$ , much further than would be expected for a flat plate or for a cylinder with a much larger value of  $a^+$ . This is a reflection of the fact that the turbulence model does not

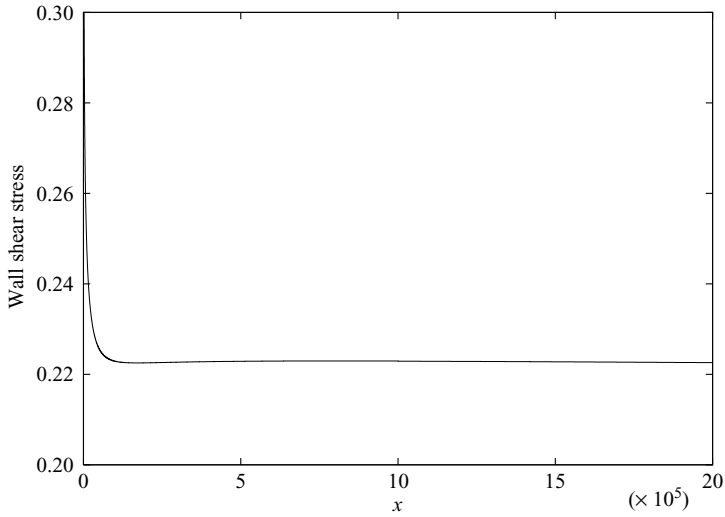


FIGURE 12. Non-dimensional wall shear stress (in units of  $\mu U_\infty/a$ ) versus distance along the cylinder (scaled on the radius  $a$ ) with  $Re = 10$ .

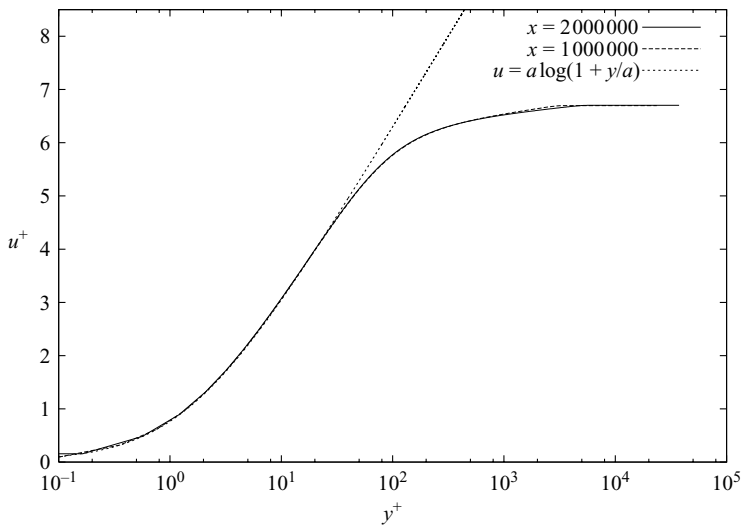


FIGURE 13. The velocity in wall units ( $u^+ = \hat{u}/\hat{u}_\tau$ ) against  $y^+ = (r-1)a\hat{u}_\tau/\nu$  for a cylinder with  $Re = 10$ . Numerical values are shown for  $x \approx 10^6$  (middle curve) and  $2 \times 10^6$  (lowest curve). Also shown is the theoretical curve  $u^+ = a^+ \log(1 + y^+/a^+)$  (top curve).

produce a significant amount of turbulent viscosity in the near-wall region, with the model predicting a laminar sublayer much larger than usual.

Luxton *et al.* (1984) considered the variation of the friction velocity with Reynolds number from a number of different sets of experimental data. They produced a fit which can be written as

$$\tau_w = 0.0121 Re^{0.8}. \tag{2.10}$$

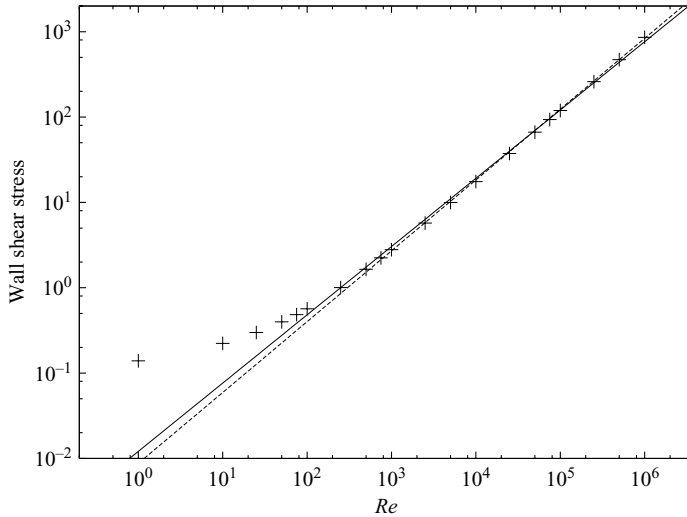


FIGURE 14. Dimensionless wall shear stress (in units of  $\mu U_\infty/a$ ) against Reynolds number. The symbols are values from the numerical model, and the lines are  $\tau_w = 0.0121 Re^{0.8}$  (solid) and  $\tau_w = 0.00876 Re^{0.83}$ .

A least-squares fit was performed for numerical values of the far downstream wall shear stress for Reynolds numbers from 200 to  $10^6$ . This gave a similar fit

$$\tau_w = 0.00876 Re^{0.83}. \quad (2.11)$$

Figure 14 shows the numerical values for the dimensionless wall shear stress versus the Reynolds number on a log–log scale. Also, shown are the predictions from (2.10) and (2.11). On the scale shown, there is little difference between (2.10) and (2.11), with both showing good agreement with the numerical values for the higher Reynolds numbers.

### 3. Navier–Stokes problem

#### 3.1. Formulation

The predictions made above using the boundary-layer model suggest a two-layer structure in the boundary layer, in which the mean properties of the flow near the wall are constant (or almost constant), while the outer flow continues to develop spatially. While it is not possible to do a Navier–Stokes solution for the full problem because of the size of the domain and computational requirement, a periodic model problem can be formulated, based on the scenario suggested by the boundary-layer results.

Consider a long cylinder with impulsively started flow along it, and suppose that we perform an unsteady boundary-layer calculation using the turbulence model as above. At any time, there will be a point along the cylinder,  $x = B(t)$  upstream of which the mean flow will be developing spatially but constant in time. Downstream of  $x = B(t)$ , the mean flow will be uniform in space but varying with time (figure 15). Denote by  $x = C$  the point downstream of which the mean wall shear stress for the fully developed flow will be constant in the steady boundary-layer calculation. If  $B(t) > C$ , the flow downstream of  $x = C$  near the wall should have constant properties in time and space. Thus, if we consider a section of the cylinder far downstream

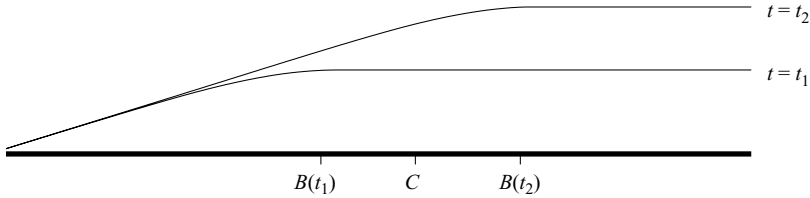


FIGURE 15. Development of the boundary layer. The point  $x = B(t)$  marks the transition between spatial and temporal behaviour of the boundary layer.  $x = C$  is the point where the wall shear stress takes a constant value.

with  $x \gg B(t) > C$ , the flow should be spatially periodic on the section, provided the section is sufficiently long.

We will consider flow on a periodic domain, developing in time. If the model presented above is correct, the wall shear stress should settle on a value close to that predicted by the boundary-layer model, and hence consistent with experimental values. Also, near the surface, the mean velocity profile should be close to that given by the boundary-layer model, as should the Reynolds stress  $-\overline{u'v'}$ . These will provide tests for the feasibility of the model.

Further, the boundary-layer model suggests that strong turbulence exists only near the wall, where there is little variation on the mean flow. Hence, the contribution to surface pressure fluctuations from this part of the flow should not vary significantly with time provided the boundary layer is thick enough, with the variation in the pressure spectra with time coming from the large-scale motions, affecting mainly the low-frequency range (see Bull (1996) or Farabee & Casarella (1991) for a discussion of frequency ranges and their scalings in wall-bounded boundary layers).

Also, when using the turbulence model but with the flow developing in time and uniform in space, the value of the wall shear stress should settle on a value close to that obtained from the spatial boundary-layer model. Figure 16 shows the result of a time-dependent calculation with  $Re = 10^3$ . There is excellent agreement with the spatial model.

The governing equations in non-dimensional form are the continuity equation

$$\frac{\partial u}{\partial x} + \frac{\partial v}{\partial r} + \frac{v}{r} + \frac{1}{r} \frac{\partial w}{\partial \phi} = 0, \quad (3.1)$$

and the Navier–Stokes equations

$$\frac{\partial u}{\partial t} + w\Omega_r - v\Omega_\phi = -\frac{\partial P}{\partial x} + \frac{1}{Re} \nabla^2 u, \quad (3.2)$$

$$\frac{\partial v}{\partial t} + u\Omega_\phi - w\Omega_x = -\frac{\partial P}{\partial r} + \frac{1}{Re} \left( \nabla^2 v - \frac{v}{r^2} - \frac{2}{r^2} \frac{\partial w}{\partial \phi} \right), \quad (3.3)$$

$$\frac{\partial w}{\partial t} + v\Omega_x - u\Omega_r = -\frac{1}{r} \frac{\partial P}{\partial \phi} + \frac{1}{Re} \left( \nabla^2 w - \frac{w}{r^2} + \frac{2}{r^2} \frac{\partial v}{\partial \phi} \right), \quad (3.4)$$

where  $\mathbf{u} = (u, v, w)$  is the velocity in polar coordinates  $(x, r, \phi)$ ,

$$\nabla^2 = \frac{\partial^2}{\partial x^2} + \frac{\partial^2}{\partial r^2} + \frac{1}{r} \frac{\partial}{\partial r} + \frac{1}{r^2} \frac{\partial^2}{\partial \phi^2}$$

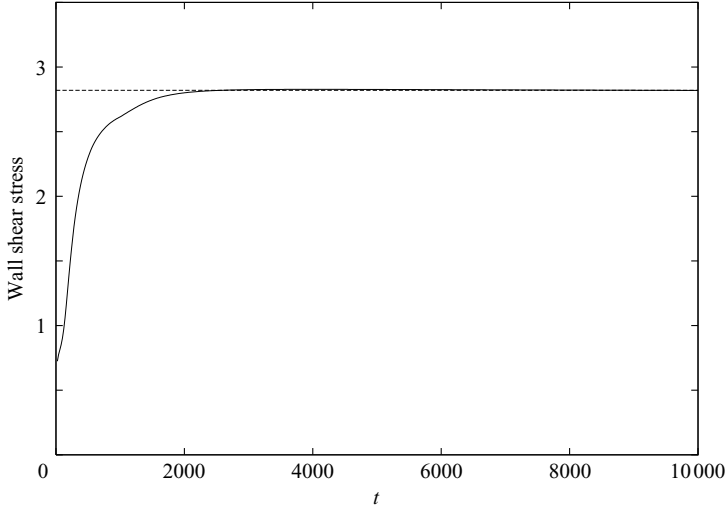


FIGURE 16. The wall shear stress (in units of  $\mu U_\infty/a$ ) against time (in units of  $a/U_\infty$ ) for a time-dependent but spatially uniform flow using the Spalart–Allmaras turbulence model.  $Re=10^3$ . The straight line gives the downstream value from the spatially developing boundary-layer model.

is the Laplacian,

$$(\Omega_x, \Omega_r, \Omega_\phi) = \left( \frac{1}{r} \frac{\partial(rw)}{\partial r} - \frac{1}{r} \frac{\partial v}{\partial \phi}, \frac{1}{r} \frac{\partial u}{\partial \phi} - \frac{\partial w}{\partial x}, \frac{\partial v}{\partial x} - \frac{\partial u}{\partial r} \right) \quad (3.5)$$

is the vorticity, and

$$P = p + \frac{1}{2} |\mathbf{u}|^2 \quad (3.6)$$

is a modified pressure. The time is written in non-dimensional form as  $t = \hat{t} U_\infty/a$ . The inertial terms in the Navier–Stokes equations (3.2)–(3.4) have been written in vorticity form as this has better numerical characteristics than the standard convective form.

The flow is calculated on a cylinder of non-dimensional length  $L$ . The boundary conditions are

$$\mathbf{u} = \mathbf{0} \quad \text{on } r = 1, \quad -\frac{1}{2}L \leq x \leq \frac{1}{2}L, \quad (3.7)$$

$$\mathbf{u} \rightarrow (1, 0, 0) \quad \text{as } r \rightarrow \infty. \quad (3.8)$$

Periodicity implies

$$\mathbf{u}\left(\frac{1}{2}L, r, \phi, t\right) = \mathbf{u}\left(-\frac{1}{2}L, r, \phi, t\right). \quad (3.9)$$

### 3.2. Numerical

The code developed for this study uses standard methods, and thus will be described in outline only. Fourier series are used in the streamwise ( $x$ ) and polar ( $\phi$ ) directions, and a second-order central difference method in the radial ( $r$ ) direction. As is usual with simulations of turbulent flow, a pseudospectral method is used, with the nonlinear terms handled explicitly and the linear terms implicitly. A second-order Adams–Bashforth method is used for the nonlinear terms, and a second-order backward difference formula is used for the time derivative. At each time step, the momentum equations are solved to obtain an intermediate velocity field. This velocity is then updated through a pressure correction substep which ensures that the continuity equation (3.1) is satisfied at each time step. As in Neves *et al.* (1992), to simplify the

numerical procedure, the cross-coupling viscous terms in (3.3) and (3.4) were included with the nonlinear terms. This does not alter the formal accuracy of the scheme.

A staggered grid was used, with the radial velocity  $v$  defined on the grid points  $r_j$  and the pressure and the other velocity components at the midpoints. Staggering the variables in this manner allows the discrete form of the continuity equation to be satisfied within rounding error. The grid in  $r$  was stretched so that the points are clustered near the surface of the cylinder.

We denote the Fourier transform of  $f$  as  $f_{j,m}^*$  where  $j$  and  $m$  are the mode numbers in  $x$  and  $\phi$ , respectively. In the far field ( $r = r_{max}$ ), the mean value of the streamwise velocity  $u_{0,0}^*$  is set to the free-stream value, and the radial derivative of the other modes of  $u$  are set to zero. The modes of the azimuthal velocity  $w$  also have a zero radial derivative, while from continuity (3.1)

$$\frac{\partial}{\partial r}(rv_{j,m}^*) = 0 \quad \text{at } r = r_{max}.$$

The mean value of the pressure  $P_{0,0}^*$  was set to zero in the far field, which provides the necessary normalization of the pressure. Again, a zero derivative condition was used for the other modes.

The scheme reduces the Navier–Stokes equations to a system of tridiagonal equations for the Fourier modes of the velocity and the pressure, second-order in time and space, which are easily solved.

An updated version of the code uses a third-order Runge–Kutta time-stepping method (Nikitin 2006), in place of the second-order Adams–Bashforth backward difference scheme used in the original code. It was not practical to repeat all the calculations described below. However, a test case was performed, using the same grid with both codes and  $Re = 10^3$ . There was no significant difference in the results. Also, the computational effort was similar. The Runge–Kutta method was more stable, so that a larger time step could be used, but this only compensated for the increased effort per time step.

An initial condition must also be specified. Initially, the streamwise velocity  $u$  was given an exponential growth from zero at the surface to the free-stream value of 1, plus a random disturbance added to all velocity components. This was sufficient to provoke transition provided the boundary layer was sufficiently thick. However, it took up to  $t = 2000$  for the flow to undergo transition and for the turbulence to become established. To avoid this unproductive computational effort, for most runs, and for all those with fine grids, the results from an existing calculation where the flow was already turbulent were used to initialize the flow.

The numerical scheme described above can be used for a direct numerical solution (DNS) of the problem in which all scales are resolved. However, at the higher Reynolds numbers studied, such a calculation was impractical because of the computational effort required. Hence for these Reynolds numbers, a large eddy simulation (LES) approach was used. In this method, the larger scales are resolved, while the effects of those that are too small to be represented on the grid are simulated by the use of a subgrid model. The subgrid model consists of an eddy viscosity term which is designed to act as a filter to provide an appropriate decay of the spectrum at higher wavenumbers.

The subgrid model used is the standard Smagorinsky model with Van Driest damping to represent the reduced growth of the small scales near the surface. The

subgrid viscosity  $\mu_{sg}$  is given by

$$\mu_{sg} = Re (c_0 \Delta)^2 D^2 S \quad (3.10)$$

where  $c_0 = 0.05$ ,  $S = (2S_{ij}S_{ij})^{1/2}$ ,  $S_{ij}$  is the rate of strain tensor, and  $\Delta = (r \Delta x \Delta r \Delta \phi)^{1/3}$  gives the characteristic local grid step.  $D$  is a wall damping function given by

$$D = 1 - \exp\left(-\frac{y^+}{A}\right), \quad (3.11)$$

where  $A = 26$ .

The subgrid model is incorporated into the numerical scheme by multiplying the viscous terms by a non-dimensional viscosity  $\mu$  where

$$\mu = 1 + \mu_{sg} \quad (3.12)$$

or

$$\mu = \max(1, \mu_{sg}). \quad (3.13)$$

An advantage of (3.13) over the usual model (3.12) is that, if the subgrid viscosity is sufficiently small,  $\mu$  will be 1, and the calculation will be DNS. For the lower Reynolds numbers considered, 2000 or less, this was the case and the LES model was not used. Swapping between (3.12) and (3.13) provides a simple method of estimating the effect of the LES model.

When the LES method was used, at each time step,  $\mu_{sg}$  was calculated for each value of  $r$  by using the strain  $S$  averaged over  $x$  and  $\phi$ , an approach used by Moin & Kim (1982). The LES model is easily incorporated into the numerical scheme using this method. Also, it is consistent with the expected behaviour of the flow, where the inner part of the boundary layer should tend to a constant state with a constant value of the wall shear stress.

It is known that the Smagorinsky model is overly dissipative with regard to the large scales in the flow. Therefore, the subgrid model was applied only to high-frequency modes, usually the top eighth, although this was varied to assess the effect of varying the LES model.

A number of tests were performed to check the code. These included analytic tests of the one-dimensional Helmholtz and Poisson solvers arising from the momentum and pressure equations, the use of known functions for the formation of the nonlinear terms, and solutions of Burgers equation to test the time stepping. Results from the code operating in planar mode were compared with those from studies of channel flow, with excellent agreement. Also, the travelling-wave solutions of Wedin & Kerswell (2004), which are unsteady, nonlinear solutions of the Navier–Stokes equations, were compared with solutions obtained from a version of the code developed for pipe flow. Again, there was good agreement.

One of the major aims of the work is to investigate the effect of the Reynolds number of the noise generated at the surface of the cylinder by the turbulent pressure fluctuations procedure. This can be measured by the power spectrum (power spectral density) of the pressure. The pressure was circumferentially averaged at a specific value of  $x$ , the data were split into a number of samples, a Hanning window was applied to each sample, normalized to ensure that the variance of the windowed data matched that of the original data, and the power spectrum was then calculated as the average over the samples.

Table 4 gives the parameters for the grids used in the Navier–Stokes calculations. This is not a complete list; other grids were used to verify the accuracy of the

$Re$	$a^+$	$J$	$K$	$M$	$L$	$L^+$	$\Delta x^+$	$\Delta \phi^+$
300	18.5	512	100	64	96	1775	3.5	1.8
500	28.7	512	100	64	96	2757	5.4	2.8
$10^3$	52.8	512	120	256	96	5070	9.9	1.3
$2 \times 10^3$	98.1	512	100	128	48	9416	9.2	4.8
$5 \times 10^3$	223.4	256	120	64	48	10 721	41.9	21.9
$5 \times 10^3$	223.4	512	120	256	24	5361	10.5	5.5
$10^4$	418.4	512	100	128	48	20 083	39.2	20.5
$10^4$	418.4	512	100	256	24	10 042	19.6	10.3
$5 \times 10^4$	1824.8	512	100	256	24	43 796	85.5	44.8
$5 \times 10^4$	1824.8	1024	100	512	24	43 796	42.8	22.4

TABLE 4. Grid parameters.  $\Delta x^+ = a^+L/J$  is the streamwise grid step and  $\Delta \phi^+ = 2\pi a^+/M$  the azimuthal grid step at the surface of the cylinder in wall units.  $L^+ = a^+L$  is the length of the cylinder in wall units.  $a^+$  is calculated using values from the boundary-layer model. Where two values are given for a particular  $Re$ , the first was used to generate the wall shear stress and the second the wall pressure spectrum.

$Re$	$\tau_{wb}$	$\tau_{wn}$	$\bar{p}_{rms}$	$p_{rms}$
300	1.14	1.38	$1.33 \times 10^{-3}$	$2.77 \times 10^{-3}$
500	1.65	1.87	$1.34 \times 10^{-3}$	$2.79 \times 10^{-3}$
$10^3$	2.79	2.91	$1.30 \times 10^{-3}$	$3.42 \times 10^{-3}$
$2 \times 10^3$	4.81	4.74	$1.28 \times 10^{-3}$	$3.62 \times 10^{-3}$
$5 \times 10^3$	9.98	9.78	$1.17 \times 10^{-3}$	$4.39 \times 10^{-3}$
$10^4$	17.5	17.2	$1.03 \times 10^{-3}$	$4.71 \times 10^{-3}$
$5 \times 10^4$	66.6	63.3	$0.84 \times 10^{-3}$	

TABLE 5. Characteristic values from the flow.  $\tau_{wb}$  and  $\tau_{wn}$  are non-dimensional values of the wall shear stress (in units of  $\mu U_\infty/a$ ) from the boundary layer and Navier–Stokes models, respectively. The r.m.s. pressure values are in units of  $\rho U_\infty^2$ , and  $\bar{p}_{rms}$  is the circumferentially averaged pressure and  $p_{rms}$  is the point pressure.

solutions, but these are the grids used to generate the plots presented below. Also, the power spectrum of the surface pressure was much more sensitive to variations in the grid than the spatially averaged wall shear stress. Hence, for the higher Reynolds numbers ( $Re = 5 \times 10^3$  and above), relatively short runs with finer grids were used to collect data to calculate the pressure spectra.

Table 5 gives values for the mean wall shear stress and the r.m.s. pressure values for the circumferentially averaged wall pressure. Also given are values for the point r.m.s. pressure where available.

The azimuthal grid step increases linearly with distance from the surface of the cylinder, leading potentially to a lack of resolution in the outer part of the flow. However, the boundary-layer results presented above strongly suggest that the major turbulent effects will be confined to a region close to the surface. Therefore, we might expect that the results will be tolerant of this increase in the grid step away from the surface. For all Reynolds numbers, at least two different values of  $M$  were used to evaluate the effects of the azimuthal grid density. Figure 17 shows power spectra for  $Re = 10^3$  with 64, 128 and 256 points azimuthally, but otherwise the same grid as in table 4. The spectra are given for the non-dimensional circumferentially averaged wall pressure against the frequency  $\omega$ , where the discrete frequencies are given by  $\omega_m = m(2\pi/T)$ , where  $T$  is the time for each sample. There is no significant difference

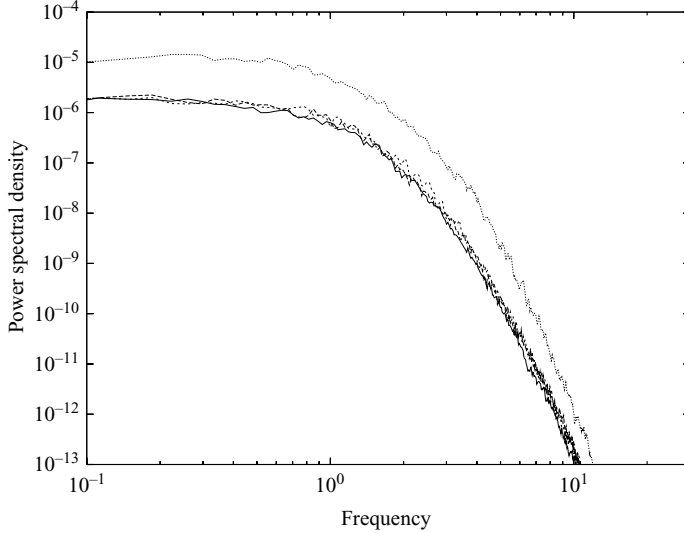


FIGURE 17. Non-dimensional power spectra for the wall pressure (in units of  $a\rho^2U_\infty^3/2\pi$ ) against frequency (in units of  $U_\infty/a$  radians) for  $Re = 10^3$ . The bottom three lines are for the circumferentially averaged pressure for  $M = 64, 128$  and  $256$ . The top line is for point pressure for  $M = 256$ .

in the spectra. The behaviour of the wall shear stress was also unaffected by the variation in  $M$ . The power spectrum for point wall pressure for  $M = 256$  is also shown in figure 17.

A number of different factors must be taken into account when selecting the size of the domain. The boundary-layer thickness will grow with time. As the largest structures in the flow would be expected to be the size of the boundary layer, the periodic model will not be valid once the boundary-layer thickness approaches the length of the domain. We are interested in thick boundary layers. In practice, this requires the non-dimensional boundary-layer thickness to be 10 or greater, which suggests that  $L$  should be at least 20. Examination of the solutions over a range of Reynolds numbers showed that once the boundary-layer thickness became much greater than half the length of the cylinder, large structures could be observed in the far field which clearly would not be independent between periods. When this occurs, the effect is felt throughout the boundary layer. In particular, assuming that the boundary layer is thick enough for the inner part of the flow to have reached a constant state, with the wall shear stress oscillating around a constant value, the level of wall shear stress will drop below this value when the boundary layer becomes too thick. Usually, following this drop, the wall shear stress levelled off again around a lower value. That this drop in the level of the wall shear stress was due to the shortness of the domain was demonstrated by performing calculations with different domain lengths, but all other parameters the same. In particular, if a solution in which the boundary-layer thickness was approaching half the length of the domain, but the wall shear stress had not dropped below its equilibrium level, was used to initialize a calculation on a longer domain, this second calculation would continue with its wall shear stress maintaining its value past the point where it would have decreased on the shorter cylinder.

In contrast, allowing the boundary layer to grow past half the length of the cylinder had little effect on the power spectrum of the surface pressure.

For the lower Reynolds numbers, it was necessary for  $L$  to be considerably greater than 20 for two reasons. First, the cylinder must be long enough to accommodate the near-wall structures in the turbulence. Secondly, we wish to investigate the effect of the size of the cylinder on the surface pressure fluctuations. This requires the Reynolds number to be varied by fixing the free-stream velocity  $U_\infty$  and varying the cylinder radius  $a$ . Since the time scale is  $a/U_\infty$ , the smaller the Reynolds number, the longer the run required in non-dimensional terms to collect sufficient data in physical time to calculate the pressure spectrum. This implies a thicker boundary layer and hence a longer cylinder, particularly as the growth of the boundary layer with time is larger at lower Reynolds numbers. Integrating the streamwise momentum equation over the domain produces

$$\frac{d}{dt}(\delta_1^2 + 2\delta_1) = \frac{2}{Re}\tau_w, \quad (3.14)$$

which with (2.10) or (2.11) implies that the growth rate of the displacement thickness will increase as  $Re$  decreases. This effect will be more pronounced at very low Reynolds numbers when (2.10)/(2.11) do not apply (see figure 14). The boundary-layer and momentum thicknesses would be expected to behave in a similar manner to the displacement thickness.

The values of  $L$  given in table 4 are sufficient to satisfy these requirements. The position of the far field boundary ( $r_{max}$ ) was chosen, depending on Reynolds number, to allow the boundary layer to grow sufficiently thick without wasted effort. Grid points were distributed radially so that there were sufficient points near the wall to resolve the inner part of the boundary layer where the turbulence is strongest. An example, for  $Re = 10^3$ , of the radial grid can be seen in figure 20. In all cases, the radial grid was chosen so that the grid step at the wall was less than one in wall units.

### 3.3. Results: $Re = 10^3$

Calculations were performed for  $Re = 10^3$  for a number of different grids and domain sizes. For this Reynolds number, a DNS calculation was performed with  $\mu_{sg} = 0$ . In general, the results from the different runs were consistent, with the wall shear stress settling on a value close to that predicted by the boundary-layer model. Figure 18 shows the spatially averaged value of the wall shear stress for two runs, with different grids azimuthally and radially. The longer run has  $r_{max} = 75$  and  $M = 64$  and the shorter,  $r_{max} = 50$  and  $M = 256$ . Axially, both are as in table 4. There is no significant difference in the behaviour of the wall shear stress for these two runs. Also, a long run was performed with  $M = 128$ , which is not shown for clarity, with similar results. The pressure spectrum was the same for all three runs (figure 17).

If the boundary-layer model is accurately modelling the Navier–Stokes problem, then they should both have the same mean streamwise velocity profile, at least near the wall. Figure 19 shows the mean velocity profiles from the Navier–Stokes calculation (averaged in  $x$  and  $\phi$ ), and the predictions from the spatial boundary-layer model, when the boundary-layer thickness is approximately 18.7. There is excellent agreement.

The Reynolds stress distribution should also match that from the boundary-layer model. Figure 20 shows the values of  $-\overline{u'v'}$  against  $r$  (averaged in  $x$ ,  $\phi$  and  $t$  for the Navier–Stokes calculations) when the boundary-layer thickness is approximately 18.7. Again there is excellent agreement.

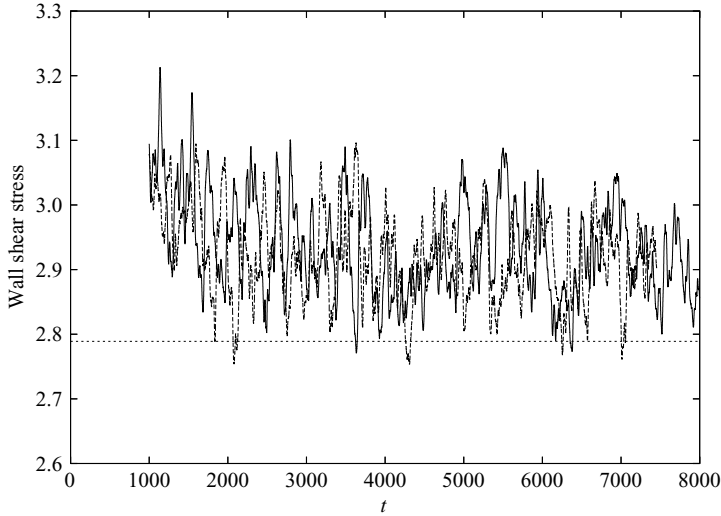


FIGURE 18. The mean wall shear stress (in units of  $\mu U_\infty/a$ ) against time (in units of  $a/U_\infty$ ) for  $Re = 10^3$ . The solid line has  $M = 64$  and the dashed line  $M = 256$ . The straight line gives the downstream value from the boundary-layer model.

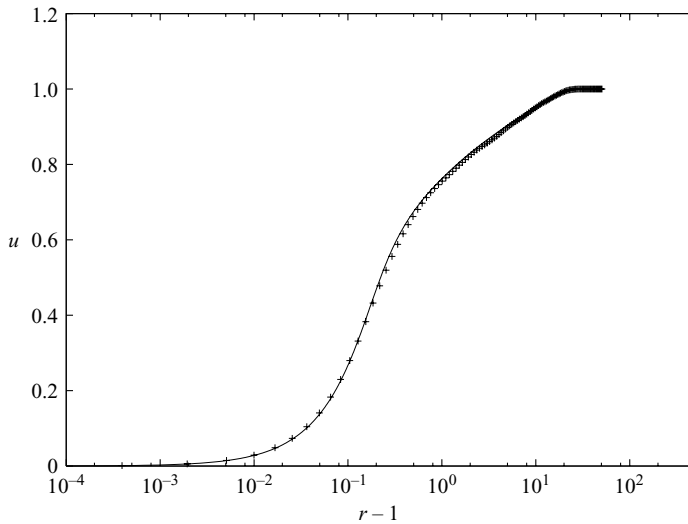


FIGURE 19. Mean streamwise velocity  $u = \hat{u}/U_\infty$  across the boundary layer (normalized by the cylinder radius  $a$ ) for  $Re = 10^3$  when  $\hat{\delta}/a \approx 18.7$ . The line is from the boundary-layer model and the symbols from the Navier–Stokes calculation.

The agreement between the boundary-layer and Navier–Stokes results shown in figures 19 and 20 is typical of comparisons made using Navier–Stokes results from a number of runs with different resolutions and with different boundary-layer thickness. Also, the variation in time of the streamwise velocity and the Reynolds stress distribution is confined mainly to the outer part of the flow, reflecting the growth of the boundary layer, consistent with the predictions from the boundary-layer model.

Experimentally, in wall-bounded flows, structures in the flow are convected at a velocity somewhat below the free-stream velocity. There are a number of ways of

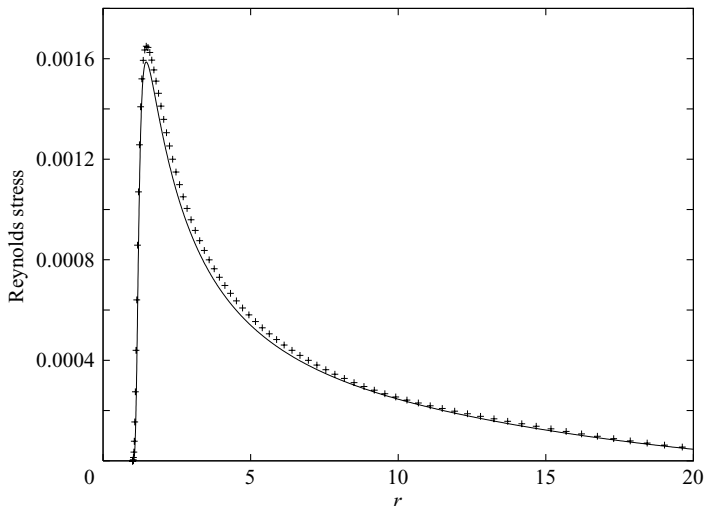


FIGURE 20. Reynolds stress  $-\overline{u'v'}$  (in units of  $U_\infty^2$ ) across the boundary layer (with distance normalized by  $a$ ) for  $Re=10^3$  when  $\hat{\delta}/a \approx 18.7$ . The line is from the boundary-layer model and the symbols from the Navier–Stokes calculation.

identifying the convection velocity. Here, we calculate the ‘coherence’ between the circumferentially averaged pressure at different points on the cylinder. We take the circumferentially averaged surface signal at two points,  $x_1$  and  $x_2$ , and calculate their spectra,  $\phi_{11}$  and  $\phi_{22}$ , and the cross-spectrum  $\phi_{12}$ , all averaged over a number of samples. The normalized magnitude of the cross-spectrum  $|\phi_{12}|/(\phi_{11}\phi_{22})^{1/2}$  gives the correlation between the two signals, while the phase of the cross-spectrum and the distance between the two measurement points may be used to estimate the convection velocity.

Figures 21 and 22 show the magnitude and phase of the coherence for signals a distance of 3 radii apart. Also shown in figure 21 are values from the empirical model formulated by Corcos (1963), which has an exponential of the form  $\exp[-c|\omega(x_2 - x_1)/U_c|]$ , where  $c=0.1$  was determined empirically. The behaviour of the coherence is consistent with those obtained experimentally for wall turbulent bounded flow as is the value of the constant  $c$  (see e.g. Farabee & Casarella 1991), and shows evidence of broadband propagation. From the phase (figure 22) and  $x_2 - x_1 = 3$ , we obtain an estimate of the convection velocity as 0.7.

Figure 23 shows contours of the two-dimensional axial wavenumber ( $\alpha$ )–frequency ( $\omega$ ) spectrum of the surface pressure fluctuation, where  $\alpha_j = j(2\pi/L)$  and  $\omega_m = m(2\pi/T)$ . The contours take the form of a narrow band (the ‘convective ridge’), consistent with the broadband propagation of structures at a well-defined convection velocity of  $U_c \approx 0.7$ . According to Taylor’s hypothesis it should be possible to relate the axial spectra ( $\Phi(\alpha)$ ) to the temporal spectra ( $\phi(\omega)$ ) through

$$\phi(\omega) = U_c \Phi(U_c \alpha). \quad (3.15)$$

Figure 24 shows a comparison between the temporal spectra calculated directly and that obtained from the spatial spectra through (3.15). There is a good level of agreement. A similar result was obtained by Neves & Moin (1994).

The convection velocity was calculated for flow with a range of Reynolds numbers. In general  $U_c \approx 0.7$ . This is consistent with the experimental results for sonar arrays

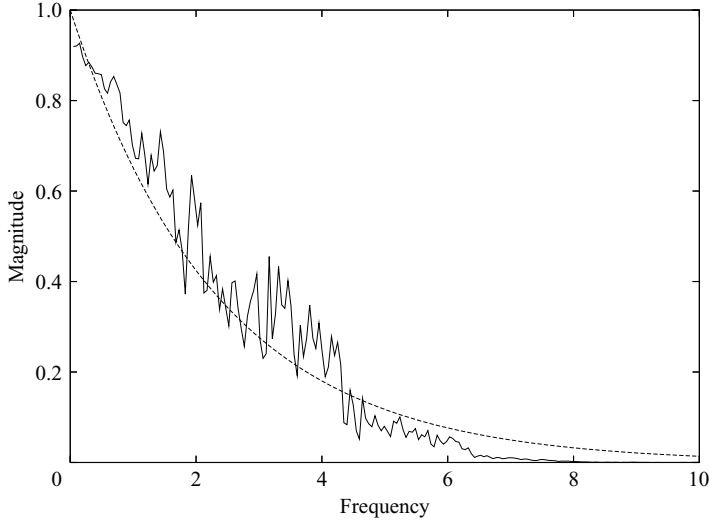


FIGURE 21. The magnitude of the coherence of the circumferentially averaged wall pressure against frequency (in units of radians  $\times U_\infty/a$ ) for  $Re = 10^3$ . The dashed line is for the Corcos model ( $\exp[-c|\omega(x_2 - x_1)/U_c|]$ ) with  $c = 0.1$ ,  $x_2 - x_1 = 3$  and  $U_c = 0.7$ .

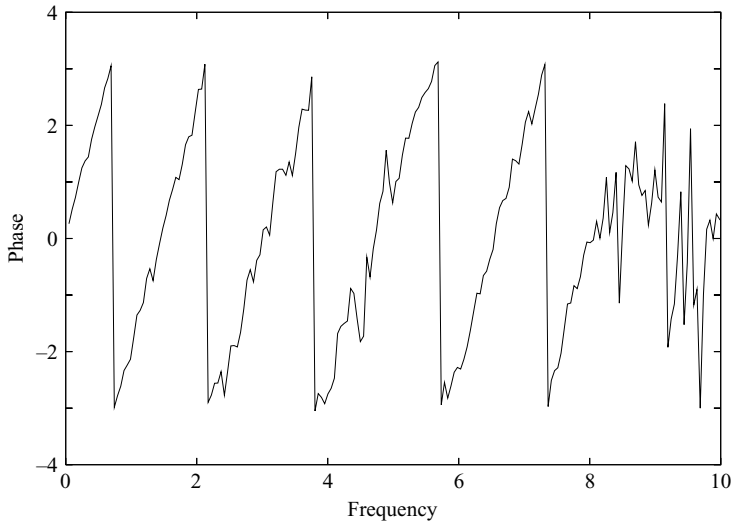


FIGURE 22. The phase of the coherence of the circumferentially averaged wall pressure (in radians) against frequency (in units of  $U_\infty/a$ ) for  $Re = 10^3$ .

of a convection velocity of 0.7 to 0.8 of the tow speed. It is slightly higher than the value obtained by Neves & Moin (1994) of around 0.65.

#### 3.4. Results: variation in Reynolds number

A detailed series of calculations were performed for Reynolds numbers from 300 to  $5 \times 10^5$ . In all cases, a number of runs were performed with different grids to check the accuracy of the results. Figure 25 shows the spatially averaged wall shear stress for  $Re = 300, 500, 1000$  and 2000, from Navier–Stokes calculations with no LES model, and the predictions from the boundary-layer model. For all three Reynolds numbers,

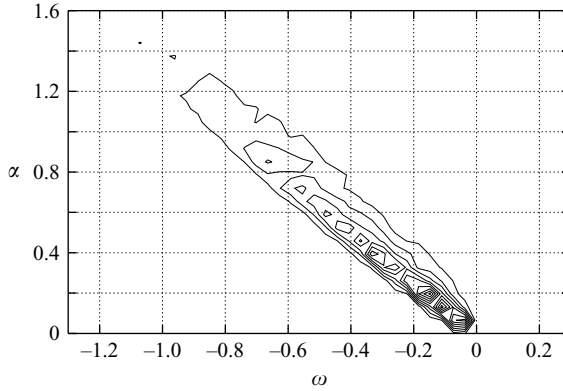


FIGURE 23. Contours of the two-dimensional axial wavenumber–frequency spectra for the circumferentially averaged wall pressure ( $\alpha - \omega$ , in units of  $a^{-1}$  radians and  $U_\infty/a$  radians, respectively).

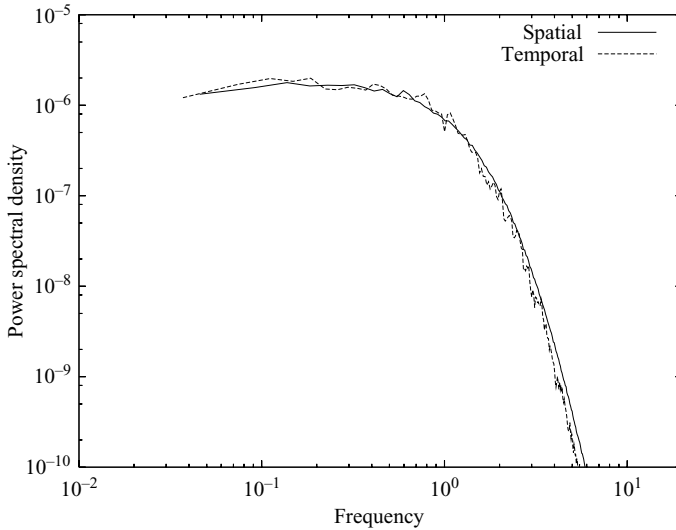


FIGURE 24. Comparison between the temporal spectra and the estimated spectra using Taylor's hypothesis (3.15) with  $U_c = 0.7$ . The spectra are for the circumferentially averaged wall pressure, and are in units of  $a\rho^2 U_\infty^3 / 2\pi$  with the frequency in units of  $U_\infty/a$  radians.

the wall shear stress eventually settles on a value close to that predicted from the boundary-layer model.

Figure 26 shows the wall shear stress for  $Re = 5000$  and  $10^4$ . For  $Re = 5000$ , calculations were performed in both DNS and LES mode with the same grid. The results from both calculations are shown in figure 26. There is no significant difference. Also, there was no significant difference in the circumferentially averaged pressure spectrum. In wall units, the grid for  $Re = 10^4$  is similar to that for  $Re = 5 \times 10^3$  (table 4), and a similar result was obtained. That is, the same level of wall shear stress and pressure spectra with and without the LES model, with good agreement with the level of wall shear stress predicted by the boundary-layer model.

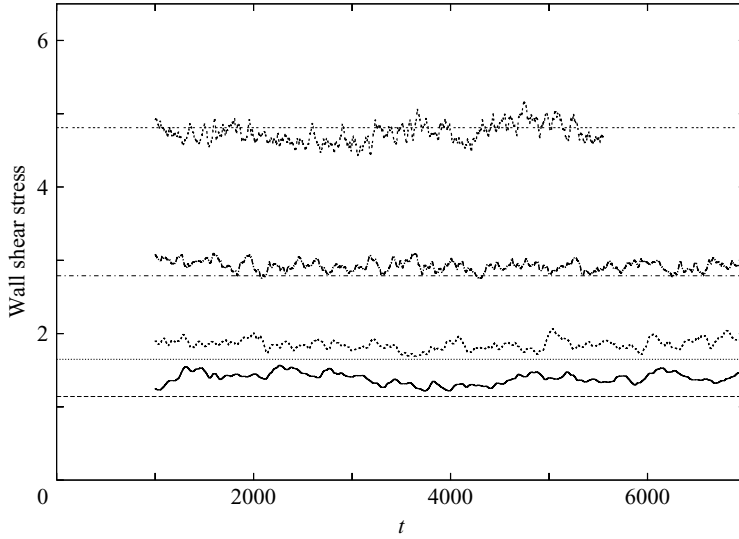


FIGURE 25. Mean wall shear stress (in units of  $\mu U_\infty/a$ ) against time (units of  $a/U_\infty$ ). From the bottom, the irregular lines are for  $Re = 300, 500, 1000$  and  $2000$ . The straight lines are the values predicted by the boundary-layer model.

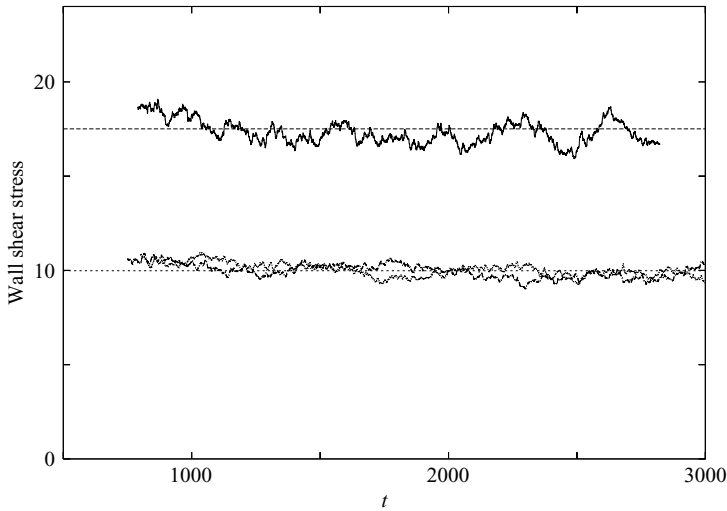


FIGURE 26. Mean wall shear stress (in units of  $\mu U_\infty/a$ ) against time (units of  $a/U_\infty$ ) for  $Re = 5000$  (bottom) and  $10^4$  (top). The straight lines are the values predicted by the boundary-layer model.

For  $Re = 5 \times 10^4$ , again the wall shear stress settled around a constant value once the boundary layer become thick enough. However, in this case, the grid used was sufficiently coarse that the details of the LES model did have some effect on the results. Figure 27 shows the wall shear stress for two runs with the same grid (as in table 4) but with  $\mu = 1 + \mu_{sg}$  and  $\mu = \max(1, \mu_{sg})$ . Both are within 10% of the value predicted by the boundary-layer model ( $\tau_w = 66.6$ ), with, not surprisingly, the lower value of the viscosity giving the higher value of wall shear stress. Again, there was no significant difference in the pressure spectra for these calculations.

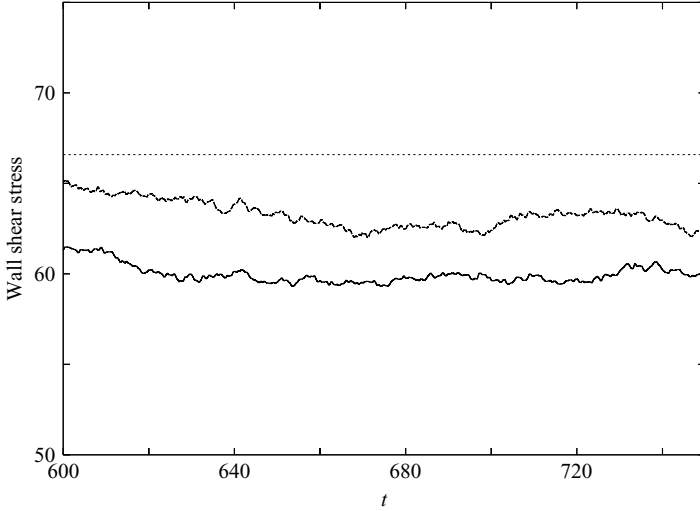


FIGURE 27. Mean wall shear stress (in units of  $\mu U_\infty/a$ ) against time (units of  $a/U_\infty$ ) for  $Re = 50000$ . The bottom line has  $\mu = 1 + \mu_{sg}$ , the middle line,  $\mu = \max(1, \mu_{sg})$ , and the top line is the value predicted by the boundary-layer model.

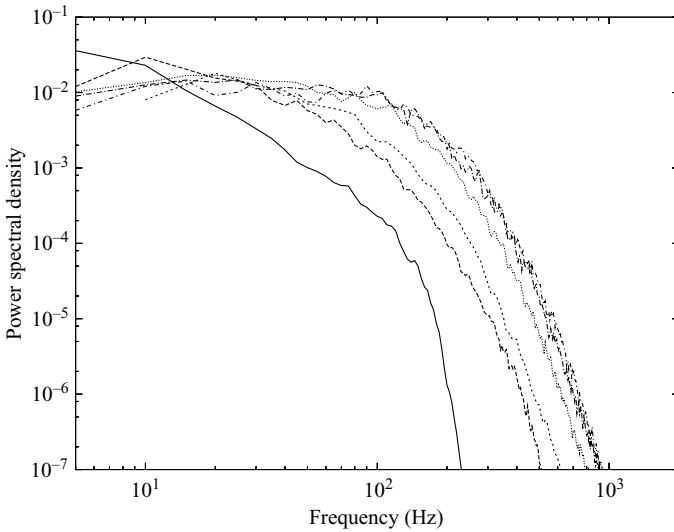


FIGURE 28. Power spectra for the circumferentially averaged surface pressure fluctuations for  $U_\infty = 1 \text{ m s}^{-1}$  and  $\nu = 1.18 \times 10^{-6} \text{ m}^2 \text{ s}^{-1}$ , in  $\text{Pa}^2 \text{ Hz}^{-1}$  against Hz. From the left, the curves are for  $Re = 5 \times 10^4, 10^4, 5 \times 10^3, 2 \times 10^3, 10^3$  and 500.

### 3.5. Pressure spectra

Pressure spectra can be presented in a number of different ways, depending on the scalings used. In this work, one of the major interests is the behaviour of the noise from the pressure fluctuations at the surface of the cylinder as the radius of the cylinder is decreased. Therefore, the pressure spectra are presented first in physical terms as  $\text{Pa}^2 \text{ s}$  against frequency in Hertz. Figure 28 gives the circumferentially averaged wall pressure power spectra for  $Re = 500$  to  $5 \times 10^4$  for flow with  $U_\infty = 1 \text{ m s}^{-1}$  and

a fluid with  $\nu = 1.18 \times 10^{-6} \text{ m}^2 \text{ s}^{-1}$ , typical of sea water. The spectra for  $Re = 5 \times 10^3$  or greater were obtained with the finer grids given in table 4. For  $Re = 5 \times 10^4$ , the streamwise and azimuthal grid steps are still relatively crude (approximately 43 and 22 in wall units, respectively), and from the results with smaller Reynolds number, where it was possible to use much finer grids in wall units, suggest that there would still be some change with further refinement of the grid. However, the results from lower Reynolds numbers also suggest that the spectrum with this resolution gives a reasonable approximation to the fully resolved spectrum, although the decay at higher frequencies may be too fast (this occurred with coarse grids at low Reynolds numbers).

As the Reynolds number/cylinder radius decreases, the pressure spectrum increases in value over a wide frequency range, consistent with the observation that the surface noise from the turbulence varies inversely with the radius of the cylinder (Marschall *et al.* 1993; Potter *et al.* 2000).

The computational effort increases as the Reynolds number drops below 500 because of the longer non-dimensional time that is required to provide data for the same physical time when the flow velocity is held constant (the scale factor is  $a/U_\infty$ ) and the larger domain required to cope with the thicker boundary layer arising from the increase in run time and the faster growth rate of the boundary layer. However, calculations were performed for  $Re = 300$ , although with a smaller number of samples, producing a spectrum with more noise than those shown in figure 28. The spectrum for  $Re = 300$  was similar to that for 500 and 1000, but has not been shown in figure 28 for clarity.

The r.m.s. pressure values (non-dimensional in units of  $\rho U_\infty^2$ ) are given in table 5. Consistent with figure 28, the r.m.s. values of the circumferentially averaged pressure increase as  $Re$  decreases, until  $Re = 500$ . The value for  $Re = 300$  is almost the same as that for 500.

When discussing pressure spectra, it is common to present them in non-dimensional form using either outer (free-stream or convection velocity and a measure of the boundary-layer thickness) or inner (friction velocity and time) variables for the scaling (see e.g. Bull 1996; Farabee & Casarella 1991). Using the outer variables does not provide any useful information as there is no significant variation in the spectra with time. In particular, for the longest run in non-dimensional terms, that with  $Re = 10^3$  and  $M = 256$ , the boundary-layer thickness approximately doubled (from around 20 to 40), but there was no significant change in either the point or circumferentially averaged pressure spectra between the first and second halves of the run. In contrast to the current situation, for wall-bounded flow, the pressure spectra for low frequencies commonly scales with the outer variables, in particular a measure of the boundary-layer thickness. One possible explanation for the lack of dependence on the boundary-layer thickness lies in the distribution of the strength of the turbulence. As shown in figures 4, 9 and 20, there is a pronounced peak in the Reynolds stress near the wall, with a rapid drop in the outer region. This suggests that the large-scale structures may be correspondingly weak, and may have much less effect on the pressure spectrum than for flow with planar geometry where the decay is less severe (see figure 4).

The wall pressure spectra were scaled using inner variables based on the friction velocity ( $\hat{u}_\tau$ ) and time ( $\nu/\hat{u}_\tau^2$ ). This involves multiplying the non-dimensional angular frequency and spectrum (as shown in figure 17) by  $\tau_w^{-1}$  and  $Re^2/\tau_w$ , respectively. Equivalently, the dimensional frequency (in Hz) and spectra (figure 28) can be multiplied by  $2\pi\nu/\hat{u}_\tau^2$  and  $\hat{u}_\tau^2/2\pi\nu\hat{\tau}_w^2$ , respectively. Circumferentially averaged pressure

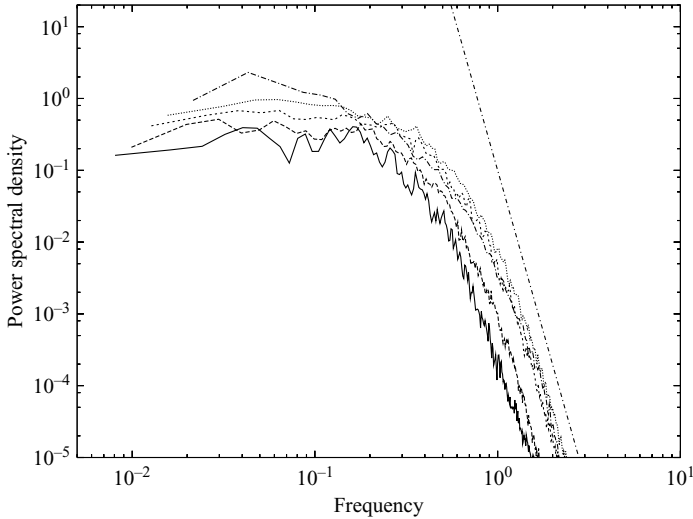


FIGURE 29. Power spectra for the circumferentially averaged surface pressure fluctuations, non-dimensionalized on the inner variables. From the bottom at low frequencies the curves are for  $Re = 300, 500, 10^3, 2 \times 10^3$  and  $10^4$ . The straight line has slope  $-9$ .

spectra scaled by the inner variables are shown in figure 29. At higher frequencies, the spectra for  $Re = 10^3$  to  $10^4$  collapse well (the curve for  $Re = 5 \times 10^3$  is omitted for clarity, but behaves in a similar manner). The curve for  $Re = 5 \times 10^4$  does not match as well, perhaps reflecting a degree of under resolution (it is also omitted for clarity). However, the curves for  $Re = 300$  and  $500$  do not match those for the higher Reynolds numbers, despite a reasonably fine grid (table 4). However, for these Reynolds numbers, the flow will not behave as typical wall-bounded flow; for  $Re = 500$ , the circumference of the cylinder is approximately 180 in wall units, and the flow would not be expected to have the usual structure with a number of streaks aligned with the flow with a typical spacing of 100 wall units and length of 1000 wall units. At small enough Reynolds number, the cylinder will interfere directly with the smallest structures in the flow, and this could lead to a fundamental change in the behaviour of the flow, and that of the wall pressure spectrum in particular.

Assume that for high frequencies the power spectra scaled on the inner variables behaves as  $\omega_i^{-m}$  where  $m > 0$  and  $\omega_i$  is the frequency scaled on the inner variables (figure 28). If we also assume that the non-dimensional wall shear stress  $\tau_w$  behaves as  $Re^n$  where  $0 < n < 1$ , as in (2.10) or (2.11), then

$$\hat{\Phi} = \kappa U_\infty^\alpha a^\beta f^{-m}, \quad (3.16)$$

where  $\hat{\Phi}$  is the dimensional power spectrum ( $\text{Pa}^2 \text{Hz}^{-1}$ ),  $f$  is the frequency in Hz,  $\alpha = (n + 1)(m + 1)$ ,  $\beta = (n - 1)(m + 1)$  and  $\kappa$  depends only on the fluid properties ( $\rho$  and  $\mu$ ). Since  $n < 1$ , (3.16) predicts that the turbulent noise as measured by the power spectrum increases as the radius of the cylinder decreases with the flow velocity held constant. Also, as expected, the turbulent noise increases as the flow velocity increases. Taking values of  $m = 9$  (figure 29) and  $n = 0.8$  (2.10 or 2.11) gives  $\alpha = 18$  and  $\beta = -2$ . That is, with the same flow conditions, the high-frequency noise from the turbulence will vary as  $O(a^{-2})$  for Reynolds numbers of  $O(10^3)$  or greater.

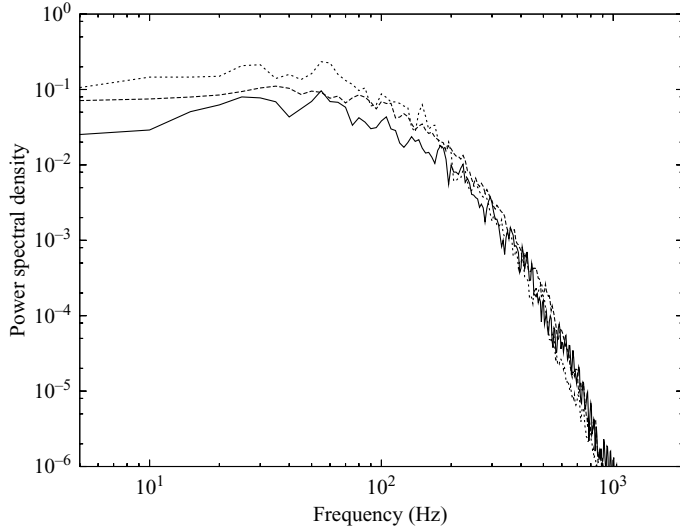


FIGURE 30. Power spectra for the point surface pressure fluctuations for  $U_\infty = 1 \text{ m s}^{-1}$  and  $\nu = 1.18 \times 10^{-6} \text{ m}^2 \text{ s}^{-1}$ , in  $\text{Pa}^2 \text{ Hz}^{-1}$  against Hz. From the bottom at low frequencies the curves are for  $Re = 300$ ,  $10^3$  and  $5 \times 10^3$ .

Figure 17 shows the point wall pressure spectra as well as the circumferentially averaged spectra for  $Re = 10^3$ . The point spectrum is approximately an order of magnitude greater than that for the circumferentially averaged pressure. This is consistent with the experimental estimates of the difference between point and averaged pressure given by Bokde *et al.* (1999) for a flow with  $Re = 3300$  and  $\hat{\delta}/a = 4.81$ . The point r.m.s. surface pressures are larger than the averaged values for all Reynolds numbers (table 5). In contrast to the circumferentially averaged values, the point r.m.s. values increase monotonically with Reynolds number (table 5), although there is little difference between the values for  $Re = 300$  and  $500$ .

Figure 30 shows surface point pressure spectra in physical terms for  $Re = 300$ ,  $10^3$  and  $5 \times 10^3$ . The curves collapse at high frequencies, but, at low frequencies, the magnitude of the spectra increases with Reynolds number. The point spectra for  $Re = 500$ ,  $2 \times 10^3$  and  $10^4$  followed this pattern, which can also be seen in the r.m.s. pressure values given in table 5 (the lines for these Reynolds numbers are omitted from figure 30 for clarity). Scaling the data for the point spectra by the inner variables separates the curves at high frequency.

Neves & Moin (1994) calculated the flow along cylinders with Reynolds numbers 311 and 674. They reported a smaller r.m.s. pressure fluctuation with the lower Reynolds number when scaled by the mean wall shear. Converting the values given by Neves & Moin (1994) into non-dimensional values scaled by  $\rho U_\infty^2$  gives  $3.39 \times 10^{-3}$  for  $Re = 674$  and  $2.83 \times 10^{-3}$  for  $Re = 311$ . The values obtained in this study for the r.m.s. point wall pressure (table 5) closely match those of Neves & Moin (1994). Snarski & Lueptow (1995) and Bokde *et al.* (1999) performed experiments at similar Reynolds numbers to those considered here. Snarski & Lueptow (1995) give a point r.m.s. wall pressure measurement (scaled on  $\rho U_0^2$ ) of  $4.32 \times 10^{-3}$  for  $Re = 3644$  for  $\delta = 5$ , and Bokde *et al.* (1999),  $4.63 \times 10^{-3}$  for  $Re = 3300$  for  $\delta = 4.81$ . These are consistent with the values obtained here (table 5).

#### 4. Conclusions

Calculations have been performed for the zero mean pressure gradient turbulent boundary layer on a long thin cylinder. The predictions using the Spalart–Allmaras turbulence model show good agreement with the experimental results over a wide range of Reynolds numbers. Both experimental and numerical results show that the boundary layer on a cylinder is thinner and has higher shear stress than for the equivalent flow on a flat plate. For all practical purposes, the shear stress on the surface of the cylinder tends to a constant downstream with the boundary layer growing in thickness as the square root of the distance. This is in marked contrast to the flow far downstream on a flat plate in which the shear continues to decay as distance to the power  $1/6$  with the boundary layer growing as distance to the power  $5/6$ .

The transverse curvature of the cylinder affects the structure of the boundary layer to an extent which depends on the Reynolds number, or equivalently, the far-downstream value of  $a^+$ . For high-Reynolds-number flows ( $O(10^5)$  or greater), the transverse curvature effects are restricted to the outer part of the boundary layer, and there is a logarithmic layer with approximately the same slope as found for the flat plate. As the Reynolds number decreases, while the log layer may still be present, its slope decreases. For Reynolds numbers of  $O(10^3)$  or less, the log layer vanishes, although the inner part of the boundary layer may still resemble that for a flat plate. Eventually, however, as the Reynolds number decreases, the effects of the transverse curvature will be felt all the way to the surface of the cylinder. At this stage, the velocity profile in the laminar sublayer will be logarithmic rather than linear.

The boundary-layer calculations suggest that when the boundary layer is sufficiently thick, the mean flow near the surface is constant (or almost constant), but continues to develop away from the wall as the boundary layer thickens. This occurs in both spatially and temporally growing flow, and is consistent with the structure suggested by Luxton *et al.* (1984) with a fine wall scale and a gross outer scale forming most of the layer. A periodic Navier–Stokes problem was formulated. The results from the Navier–Stokes/LES calculations were consistent with those of the boundary-layer model and experiments. Both the boundary layer and Navier–Stokes models show that the turbulence intensity peaks near the wall and drops off rapidly in the far field. Given the increase in area with distance away from the wall, this might be expected.

Circumferentially averaged pressure spectra were calculated from the Navier–Stokes results. These showed an increase in the surface noise from the turbulence as the Reynolds number (cylinder radius) decreased, consistent with the behaviour of sonar arrays. The results (figure 28 and table 5) indicate that the (circumferentially averaged) turbulent noise on the surface of the cylinder stops increasing when the Reynolds number is  $O(10^3)$ , i.e. with small cylinders in physical terms. In sea water,  $Re = 10^3$  corresponds to a cylinder with a radius of less than 1 mm in sea water when  $U = 1 \text{ m s}^{-1}$  or 0.1 mm when  $U = 10 \text{ m s}^{-1}$ . In air, the radius would be approximately 1.6 mm with  $U = 30 \text{ m s}^{-1}$ .

The r.m.s. values for the circumferentially averaged surface pressure followed the patterns of the spectra, increasing as the Reynolds number decreased (table 5). In contrast, the r.m.s. values for the point pressure increased with an increase in the Reynolds number.

In addition to the results presented above, some calculations were performed for Reynolds numbers up to  $2.5 \times 10^5$  using the LES model. Although the grid used in these calculations was crude, reasonable agreement (within 20%) was obtained

with the wall shear stress predicted by the boundary-layer model, and the predicted surface noise from the circumferentially averaged pressure dropped significantly as the Reynolds number increased.

Finally, we note that there was little variation in the wall pressure spectra with time, and hence with the boundary-layer thickness. The analogous result for a spatial flow developing along the cylinder would be a flow showing little variation with distance downstream.

#### REFERENCES

- BOKDE, A. L. W., LUEPTOW, R. M. & ABRAHAM, B. 1999 Spanwise structure of wall pressure on a cylinder in axial flow. *Phys Fluids* **11**, 151–161.
- BULL, M. K. 1996 Wall-pressure fluctuations beneath turbulent boundary layers: some reflections on forty years of research. *J. Sound Vib.* **190**, 299–315.
- CIPPOLA, K. M. & KEITH, W. L. 2003a High Reynolds number thick axisymmetric turbulent boundary layer measurements. *Exps. Fluids* **35**, 477–485.
- CIPPOLA, K. M. & KEITH, W. L. 2003b Momentum thickness measurements for thick turbulent axisymmetric boundary layers. *Trans. ASME I: J. Fluids Engng* **125**, 569–575.
- CORCOS, J. M. 1963 Resolution of pressure in turbulence. *J. Acoust. Soc. Am.* **35**, 192–199.
- DENLI, N. & LANDWEBER, L. 1979 Thick axisymmetric turbulent boundary layer on a circular cylinder. *J. Hydronautics* **13**, 92–104.
- FARABEE, T. M. & CASARELLA, M. J. 1991 Spectral features of wall pressure fluctuations beneath turbulent boundary layers. *Phys. Fluids A* **10**, 2410–2420.
- FUREY, D., CIPPOLA, K. M. & ATSAVAPPRANEE, P. 2004 Investigation of the turbulent boundary layer flow on a microfilament towed array. In *Proc. 25th Symp. on Naval Hydrodynamics*. St Johns, Canada.
- GLAUERT, M. B. & LIGHTHILL, M. J. 1955 The axisymmetric boundary layer on a long thin cylinder. *Proc. R. Soc. Lond. A* **224**, 188–203.
- KNIGHT, A. 1996 Flow noise calculations for extended hydrophones in fluid and solid-filled arrays. *J. Acoust. Soc. Am.* **100**, 245–251.
- LUEPTOW, R. M. 1988 Turbulent boundary layer on a cylinder in axial flow. *Tech. Rep.* 8389. US NUSC Tech. Mem.
- LUEPTOW, R. M. 1990 Turbulent boundary layer on a cylinder in axial flow. *AIAA J.* **28**, 1706–1706.
- LUEPTOW, R. M. & HARITONIDIS, J. H. 1987 The structure of the turbulent boundary layer on a cylinder axial flow. *Phys. Fluids* **30**, 2993–3005.
- LUEPTOW, R. M. & JACKSON, C. P. 1991 Near-wall streaky structure in a turbulent boundary layer on a cylinder. *Phys Fluids* **3**, 2822–2824.
- LUEPTOW, R. M., LEEHEY, P. & STELLINGER, T. 1985 The thick, turbulent boundary layer on a cylinder: mean and fluctuating velocities. *Phys Fluids* **28**, 3495–3505.
- LUXTON, R. M., BULL, M. K. & RAJAGOPALAN, S. 1984 The thick turbulent boundary layer on a long fine cylinder in axial flow. *Aero. J.* **88**, 186–199.
- MARSHALL, R. A., STINSON, D. L., PEARCE, R. E., BOYER, E. & EMBURY, B. 1993 The use of an innovative solid towed array for exploring the Antarctic marine environment. In *Proc. Oceans 93; Engineering in Harmony with Ocean*, vol. 2, pp. II/35–II/40.
- MOIN, P. & KIM, J. 1982 Numerical investigation of turbulent channel flow. *J. Fluid Mech.* **118**, 341–377.
- NEPOMUCENO, H. G. & LUEPTOW, R. M. 1997 Pressure and shear stress measurements at the wall in a turbulent boundary layer on a cylinder. *Phys Fluids* **9**, 2732–2739.
- NEVES, J. C. & MOIN, P. 1994 Effects of convex transverse curvature on wall bounded turbulence. Part 2. The pressure fluctuations. *J. Fluid Mech* **272**, 383–406.
- NEVES, J. C., MOIN, P. & MOSER, R. D. 1992 Numerical study of axial turbulent flow over long cylinders. *Tech. Rep.* 54. Department of Mechanical Engineering, Stanford University.
- NEVES, J. C., MOIN, P. & MOSER, R. D. 1994 Effects of convex transverse curvature on wall bounded turbulence. Part 1. The velocity and vorticity. *J. Fluid Mech* **272**, 349–381.

- NIKITIN, N. 2006 Third-order accurate semi-implicit Runge–Kutta scheme of the incompressible Navier–Stokes equations. *Intl J. Numer. Meth. Fluids* **51**, 221–233.
- POTTER, J. R., DELORY, E., CONSTANTIN, S. & BADIU, S. 2000 The ‘thinarray’: a lightweight, ultra-thin (8 mm OD) towed array for use with small vessels of opportunity. In *Proc. Intl Symp. on Underwater Technology*, pp. 49–53. Tokyo.
- SEBAN, R. A. & BOND, R. 1951 Skin-friction and heat-transfer characteristics of a laminar boundary layer on a cylinder in axial compressible flow. *J. Aero. Sci.* **18**, 671–675.
- SNARSKI, S. R. & LUEPTOW, R. M. 1995 Wall pressure and coherent structures in a turbulent boundary layer on a cylinder in axial flow. *J. Fluid Mech.* **286**, 137–171.
- SPALART, P. R. & ALLMARAS, S. R. 1994 A one-equation turbulence model for aerodynamic flows. *Recherche Aerospaciale* **1**, 5–21.
- STEWARTSON, K. 1955 The asymptotic boundary layer on a circular cylinder in axial incompressible flow. *Q. Appl. Maths* **13**, 113–122.
- TUTTY, O. R., PRICE, W. G. & PARSONS, A. T. 2002 Boundary layer flow on a long thin cylinder. *Phys. Fluids* **14**, 628–637.
- WEDIN, H. & KERSWELL, R. R. 2004 Exact coherent structures in pipe flow: travelling wave solutions. *J. Fluid Mech.* **508**, 333–371.
- WIETRZAK, A. & LUEPTOW, R. M. 1994 Wall shear stress and velocity in a turbulent axisymmetric boundary layer. *J. Fluid Mech.* **259**, 191–218.
- WILLMARTH, W. W. & YANG, C. S. 1970 Wall-pressure fluctuations beneath turbulent boundary layers on a flat plate and a cylinder. *J. Fluid Mech.* **41**, 47–80.
- WILLMARTH, W. W., WINKEL, R. E., SHARMA, L. K. & BOGAR, T. J. 1976 Axially symmetric turbulent boundary layers on cylinders: mean velocity profiles and wall pressure fluctuations. *J. Fluid Mech.* **76**, 35–64.